JOURNAL OF GEOPHYSICAL RESEARCH, VOL. 98, NO. C6, PAGES 10,085–10,109, JUNE 15, 1993

An Intermediate One-Dimensional Thermodynamic Sea Ice Model for Investigating Ice-Atmosphere Interactions

ELIZABETH E. EBERT

Bureau of Meteorology Research Centre, Melbourne, Australia

JUDITH A. CURRY

Department of Aerospace Engineering Sciences, Boulder, Colorado

A one-dimensional thermodynamic model of sea ice is presented that focuses on those features that are most relevant to interactions with the atmosphere, namely the surface albedo and leads. It includes a surface albedo parameterization that interacts strongly with the state of the surface, and explicitly includes meltwater ponds. The lead parameterization contains a minimum lead fraction, absorption of solar radiation in and below the leads, lateral accretion and ablation of the sea ice, and a prescribed sea ice divergence rate. The model performed well in predicting the current climatic sea ice conditions in the central Arctic when compared with observations and other theoretical calculations. Results of parameter sensitivity tests produced large equilibrium ice thicknesses for small values of ice divergence or large values of minimum lead fraction as a result of positive feedback mechanisms involving cooling of water in the leads. The ice thickness was also quite sensitive to the meltwater runoff fraction and moderately sensitive to the other parameters in the melt pond parameterization, a result of the strong dependence of the surface albedo, and hence the net flux, on the surface conditions. To further investigate the physical interactions and internal feedback processes governing the sea ice-lead system, sensitivity tests were also performed for each of the external forcing variables. The model's equilibrium sea ice thickness was extremely sensitive to changes in the downward longwave and shortwave fluxes and atmospheric temperature and humidity, moderately sensitive to the value of the ocean heat flux, and insensitive to values of wind speed, snowfall, and rainfall in the immediate vicinity of the baseline forcing, although significant changes in thickness occurred for larger variations in wind speed and snowfall. Four important positive feedback loops were identified and described: (1) the surface albedo feedback, (2) the conduction feedback, (3) the lead solar flux feedback, and (4) the lead fraction feedback. The destabilizing effects of these positive feedbacks were mitigated by two strong negative feedbacks: (1) the outgoing longwave flux feedback, and (2) the turbulent flux feedback. Considering the strong influence which sea ice has on global atmospheric and oceanic circulation patterns, it is essential that climate models be able to treat these feedback processes appropriately.

1. INTRODUCTION AND BACKGROUND

The configuration of sea ice significantly influences variations of the atmospheric and oceanic circulation patterns on all spatial and temporal scales. A survey of sea ice-atmosphere interaction processes occurring on different scales has been given by *Walsh* [1983]. Variations in snow and ice cover play a crucial role in climate via the following physical processes: (1) the formation of ice causes a much larger portion of the incoming solar energy to be reflected back to space, (2) the formation of ice reduces the transfer of sensible and latent heat between the ocean and atmosphere, (3) because of the latent heat associated with melting and freezing, sea ice acts as a thermal reservoir which delays the seasonal temperature cycle, and (4) the formation of sea ice alters the ocean salinity and hence the ocean density stratification by the expulsion of brine during freezing and by the large-scale transport of low-salinity ice.

The horizontal extent and the vertical thickness of sea ice are determined by both thermodynamic processes (freezing and melting) and dynamic processes (sea ice drift and deformation). Freezing and melting are primarily influenced by radiation and heat exchanges with the atmosphere and ocean, whereas the sea ice motion is dominated by momentum transfers from the atmosphere and ocean and by internal ice stress. The thermodynamic processes occurring in sea ice are best described by *Maykut and Untersteiner* [1971] (hereinafter referred to as MU). Using a one-dimensional thermodynamic model of sea ice, MU modeled the time-dependent vertical diffusion process occurring within the ice, using prescribed heat fluxes at the atmospheric and oceanic boundaries. The MU model included the effects of internal heating due to penetrating solar radiation and the internal storage of heat in brine pockets, and allowed variation of the specific heat and thermal conductivity of the ice with temperature.

A model that includes the essential physics of sea ice dynamics is described by *Hibler* [1979]. Sea ice dynamics are largely responsible for the distributions of ice thickness and compactness. Ice may be transported into regions where it might not occur by thermodynamic processes alone, leaving open spaces behind which are referred to as "leads." During winter, leads freeze over, resulting in an increase in the total area covered by ice. During the summer, leads enlarge laterally through the absorption of solar radiation, causing a more rapid reduction in ice coverage. In addition, long-term patterns of ice drift result in large-scale advective transports of heat and salinity. Model simulation results by *Hibler* [1979] show that this lateral heat transport can be of the same magnitude as the net vertical heat fluxes over perennial ice. Generally, sea ice thermodynamics and dynamics are intrinsically related: the freezing rates in winter depend on the ice thickness; ice thickness depends on the ice velocity pattern; and the sea ice velocity is modified by the distribution of thin and thick ice.

Since the susceptibility of the Arctic ice to a global warming was first pointed out by *Budyko* [1962], numerical climate models have increasingly included sea ice prediction schemes. While a combination of the MU and Hibler models possesses most of the

Paper number 93JC00656.
0148-0227/93/93JC-00656$05.00

important physical processes required for modeling sea ice, these models are too computationally intensive to be used in climate simulations. As a result, numerous simplifications to these models have been proposed. Earlier sea ice models that were formulated for climate simulations accounted only for the thermodynamic processes and neglected sea ice drift and deformation, assuming that dynamic effects are small on climatic temporal and spatial scales. A simplified version of the MU model that retains most essential components was proposed by *Semtner* [1976]; this version reduced the number of layers to three, eliminated the heat source term in the diffusion equation, and fixed the specific heat and conductivities of snow and ice. *Semtner* [1976] also proposed a zero-layer version, which is essentially a linear formulation of a sea ice model with a snow cover on top of the ice. In large-scale simulations of sea ice, *Washington et al.* [1976], *Parkinson and Washington* [1979], and the CO_2 doubling study of *Parkinson and Kellogg* [1979] have all used Semtner's zero-layer formulation. These three experiments were undertaken with prescribed atmospheric forcing (no feedbacks with the atmosphere), with the last two experiments including limited sea ice dynamical effects. These models have done a reasonable job of simulating the annually averaged present day sea ice characteristics. In an experiment where surface temperature was increased by 5°C (corresponding to a temperature increase expected for CO_2 doubling), *Parkinson and Kellogg* [1979] found that the sea ice would completely melt during summer in each hemisphere, the ice reappearing in winter.

Manabe and Stouffer [1980] and *Washington and Meehl* [1983] conducted the first climate experiments that included feedbacks between the sea ice and the atmosphere, using simpler formulations of sea ice thermodynamics than even Semtner's zero-layer formulation. When the CO_2 concentrations were quadrupled [*Manabe and Stouffer*, 1980], the ice disappeared completely from the Arctic for several summer months each year. Near-surface temperature changes in the central Arctic were modeled to be 13°C in winter and 4°C in summer. Reasons given for the large warming in high latitudes were associated with the albedo-temperature feedback, increased atmospheric moisture content, and stronger stability of the polar atmosphere.

Semtner [1984] showed that phase and amplitude of the seasonal sea ice cycle are in error for the zero-layer thermodynamic sea ice model, exaggerating the seasonal cycle of sea ice. Use of the zero-layer model (and presumably simpler models) may therefore lead to erroneous conclusions about the magnitude of climate change in the polar regions. In a calculation using his three-level thermodynamic sea ice model, *Semtner* [1984] showed that quadrupling CO_2 did not result in a summertime melting of the Arctic sea ice, in contrast to the *Parkinson and Washington* [1979] and *Manabe and Stouffer* [1980] results.

Because of the complexity of simulating ice dynamics [e.g., *Hibler*, 1979; *Hibler and Walsh*, 1982], relatively little attention has been given to incorporating the dynamics of sea ice in general circulation models. The first to include a simple account of ice dynamics in a climatic simulation of sea ice were *Parkinson and Washington* [1979], who included a lead parameterization. Increasingly sophisticated sea ice parameterizations of ice dynamics in simple thermodynamic models of sea ice have been included in the energy balance climate models of *Ledley* [1988] and *Harvey* [1988*b*], who have further emphasized the importance of leads in climate. The coupled ocean-ice models of *Hibler and Bryan* [1987], *Semtner* [1987], and *Mellor and Kantha* [1989] have included ice dynamics to varying degrees, but the atmospheric forcing has been specified in these calculations. It is noted that for a perturbation experiment with atmospheric temperatures increased by 2°C in all months, *Semtner* [1987] found that the Arctic ice disappeared for 1 month in late summer, although it reformed in winter; this is in disagreement with the results of *Semtner* [1984] using only a thermodynamic sea ice calculation. The recent parameterization of ice rheology formulated by *Flato and Hibler* [1992] for the first time allows a sophisticated formulation of sea ice dynamics to be included in atmospheric general circulation models (GCMs).

The present paper considers whether existing treatments of the thermodynamics of sea ice and the modeled thermodynamic feedbacks occurring between the atmosphere and the sea ice are adequate for purposes of quantitative prediction of climate change in polar regions. Even the MU model, which contains the most sophisticated treatment of thermodynamic processes and has been considered by many to be "reality" [e.g., *Semtner*, 1984], has several deficiencies and uncertainties:

1. In the MU model, surface albedo was specified as an external parameter. While there is little disagreement about spring and autumn albedos, there is considerable question about the value of summertime melting ice albedo of 0.64 used by MU. Owing to the effect of melt ponds, summertime ice albedo is observed to be more like 0.5 [e.g., *Scharfen et al.*, 1987]. The relatively small amount of annual surface ablation modeled by MU relative to other thermodynamic calculations is a direct result of the high value of surface albedo that they used. The substantial sensitivity of thermodynamic sea ice models to surface albedo parameterization was illustrated by *Shine and Henderson-Sellers* [1985].

2. MU assumed that 17% of the absorbed solar radiation penetrated into the ice interior. This value is substantially smaller than the value of 32% determined by *Untersteiner* [1964] and the 18-35% measured by *Grenfell and Maykut* [1977]. This percentage of penetrating solar radiation has been shown to depend on the relative proportion of diffuse to direct radiation.

3. A constant value of 2 W m^{-2} for the ocean heat flux was used by MU. Observations of *Aagaard et al.* [1981] and *Perovich and Maykut* [1990] suggest that the magnitude of the basal heat flux at the bottom of the pack ice is determined almost completely by solar radiation transmitted through the ice pack (particularly through leads), rather than by the influx of warm Atlantic water through Fram Strait, as assumed by MU.

While acknowledging the uncertainties in these parameters, MU justified their choices by virtue of these values yielding model results that agreed with observations. However, *Shine and Henderson-Sellers* [1985] pointed out that the degree of uncertainty in virtually all aspects of the energy balance of the sea ice is so great that it is possible to achieve reasonable ice thickness by holding fixed one set of fluxes or parameters and by seemingly legitimate tuning of the others. They focused on the sensitivity of the sea ice to changes in surface albedo. Unlike most climate models, which parameterize sea ice albedo as a simple function of surface temperature, Shine and Henderson-Sellers modeled the albedo to be a function of the surface state, snow and ice thickness, and cloud cover, which affects both the spectral distribution of the incoming radiation and the proportions of direct and diffuse solar radiation. Using their albedo parameterization with Semtner's three-layer model, they found that the use of different albedo values for dry snow, melting snow, and bare ice, as well as careful treatment of the effect of clouds on the spectral distribution of the solar flux, had a large influence on the predicted sea ice thickness.

In addition to modeling the physical processes of the sea ice itself correctly, a key aspect of a coupled atmosphere-ocean model is to determine the feedbacks occurring between sea ice and atmosphere.

This is of particular importance for simulations of climatic change. The prediction of ice thickness is dependent on all components of the surface energy balance. In particular, the radiative fluxes at the surface play an important role in the growth and decay of sea ice and in the location of the sea ice margin [*Shine and Crane*, 1984]. Interactions between the sea ice and the atmosphere range from the strong and instantaneous local feedback between sea ice and the overlying atmospheric boundary layer, to feedbacks related to the growth and decay of ice sheets occurring on time scales of thousands of years as a result of elimination of the moisture source for snowfall if ice covers the ocean. As a result of the shortcomings in the parameterization of sea ice in existing climate models, the stability of the present sea ice cover to a specified climate perturbation is not well defined [*World Climate Research Program (WCRP)*, 1987; *Ingram et al.*, 1989]. In particular, the duration of any potential transition between a permanently and a seasonally ice-covered ocean is uncertain. The possible changes in high- latitude cloudiness as frozen sea ice is replaced by open ocean or melting ice are unknown. Climate model simulations of high- latitude cloudiness have been poor, and the feedbacks occurring between clouds and sea ice are poorly understood [*Crane and Barry*, 1984].

In this paper we present a one-dimensional thermodynamic model of sea ice that revisits the detailed thermodynamic processes occurring in sea ice on the level of the MU model. The emphasis in this paper is on thermodynamic processes, although we realize that a complete description of sea ice behavior would include a more complete treatment of sea ice dynamics. Although the trend is toward developing increasingly simple sea ice parameterizations for use in climate models, it is clear from the preceding discussion that a step back should be taken to examine the sensitivities of sea ice physical processes using a model that is more accurate than that of MU.

Our model focuses on those features which are most relevant to interactions with the atmosphere, namely the surface albedo and leads. We introduce a new surface albedo parameterization that interacts strongly with the state of the surface. Like *Shine and Henderson-Sellers'* [1985] parameterization, the albedo is dependent on surface type, snow and ice depth, and cloud cover, and it treats the solar radiation in multiple spectral intervals. An essential feature is a new melt pond parameterization which models the mass and energy balance of meltwater ponds of variable extent and depth. Because of their low albedo relative to that of bare ice, the melt ponds have a strong influence on the aerially averaged surface albedo in midsummer, enhancing the absorption of incoming solar radiation. Latent heat is returned to the ice when the ponds refreeze, retarding cooling at the surface in the fall.

Although this one-dimensional model cannot represent the motion and deformation of sea ice due to dynamic processes, it does account for many of the interactions between dynamics and thermodynamics by including a lead parameterization. Essential features of the lead parameterization include (1) a minimum lead fraction, which represents the creation of open water in winter due to wind stress and ridging, (2) absorption of solar radiation in and below the leads, which warms the ocean mixed layer and contributes to a time-varying heat flux at the base of the sea ice, (3) lateral accretion and ablation of the sea ice in response to the lead surface energy balance, and (4) a prescribed sea ice divergence rate, which represents the zonally averaged transport of ice out of the Arctic Basin.

The baseline simulation was performed here and in an earlier study [*Curry and Ebert*, 1992] by coupling the sea ice model to a cloud radiation model, producing an internally consistent set of radiative fluxes. These radiative fluxes, along with seasonal cycles of atmospheric temperature, humidity, wind speed, and precipitation, are all prescribed in our model experiments. Thus sea ice-atmosphere feedbacks are not explicitly considered in this study.

The sea ice model is described in section 2, and the predicted annual cycles of sea ice thickness, surface albedo, and several other variables, are compared with observations and other calculations in section 3. In section 4 the sensitivity of the model to values of the model parameters and variations in external forcing is examined with the purpose of defining and describing the important physical processes and feedbacks internal to the system of sea ice and leads. Conclusions are presented in section 5.

2. THE SEA ICE MODEL

The foundation for our sea ice model is the one-dimensional thermodynamic sea ice model of MU. New features include an albedo parameterization which is highly sensitive to the surface state, including a melt pond parameterization which allows for a fractional area of meltwater ponds of variable depth during midsummer. A lead parameterization and prescribed sea ice divergence rate partially account for the effects of ice dynamics. The inclusion of leads also allows for the absorption of solar radiation in the ocean, resulting in a more realistic time-varying basal heat flux at the lower surface of the ice.

The model configuration is shown in Figure 1 (The notation used in Figure 1 and throughout the paper is listed in the notation section.) It consists of a horizontally homogeneous slab of ice with a layer of snow on the surface throughout most of the year. The depth of the ice, h_i, and the depth of the snow layer, h_s, are computed as functions of the precipitation and the energy balances at the upper and lower surfaces. In summer the melting ice surface has a fraction P of meltwater ponds of depth h_p. The sea ice floats atop an ocean mixed layer of depth d_w and temperature T_w. A variable fraction, A, of leads allows energy exchange between the ocean and atmosphere.

The model is forced using prescribed spectral downward shortwave and longwave fluxes and precipitation, described later in this section. The annual cycle of Arctic sea ice evolution is simulated by repeatedly time-marching the model from January 1 to December 31, starting with the January 1 sea ice thickness and temperature profile corresponding to MU's equilibrium sea ice conditions. A time step of 8 hours is used, after MU. Equilibrium is considered to be achieved when the annually averaged ice thickness changes by less than 1 mm. The typical integration time is 10-50 years, depending on the values of the model parameters and forcing variables (section 4).

2.1. *Sea Ice Growth and Decay*

The sea ice temperature and thickness are controlled by the conduction of heat through the ice slab and the balance of fluxes at its upper and lower surfaces. The internal temperature of the ice is governed by the one-dimensional heat equation,

$$(\rho c)_i \frac{\partial T_i}{\partial t} = k_i \frac{\partial^2 T_i}{\partial z^2} = \frac{\partial F_c}{\partial z} \qquad (1)$$

where $(\rho c)_i$ is the volumetric heat capacity of ice, k_i is the sea ice thermal conductivity, and F_c is the upward conductive flux. The temperature profile is determined by numerically solving the heat equation using the Dufort-Frankel algorithm, which is an explicit, absolutely stable method (see, for example, *Mitchell and Griffiths* [1980]). Ten levels in the ice slab are used in the numerical integration.

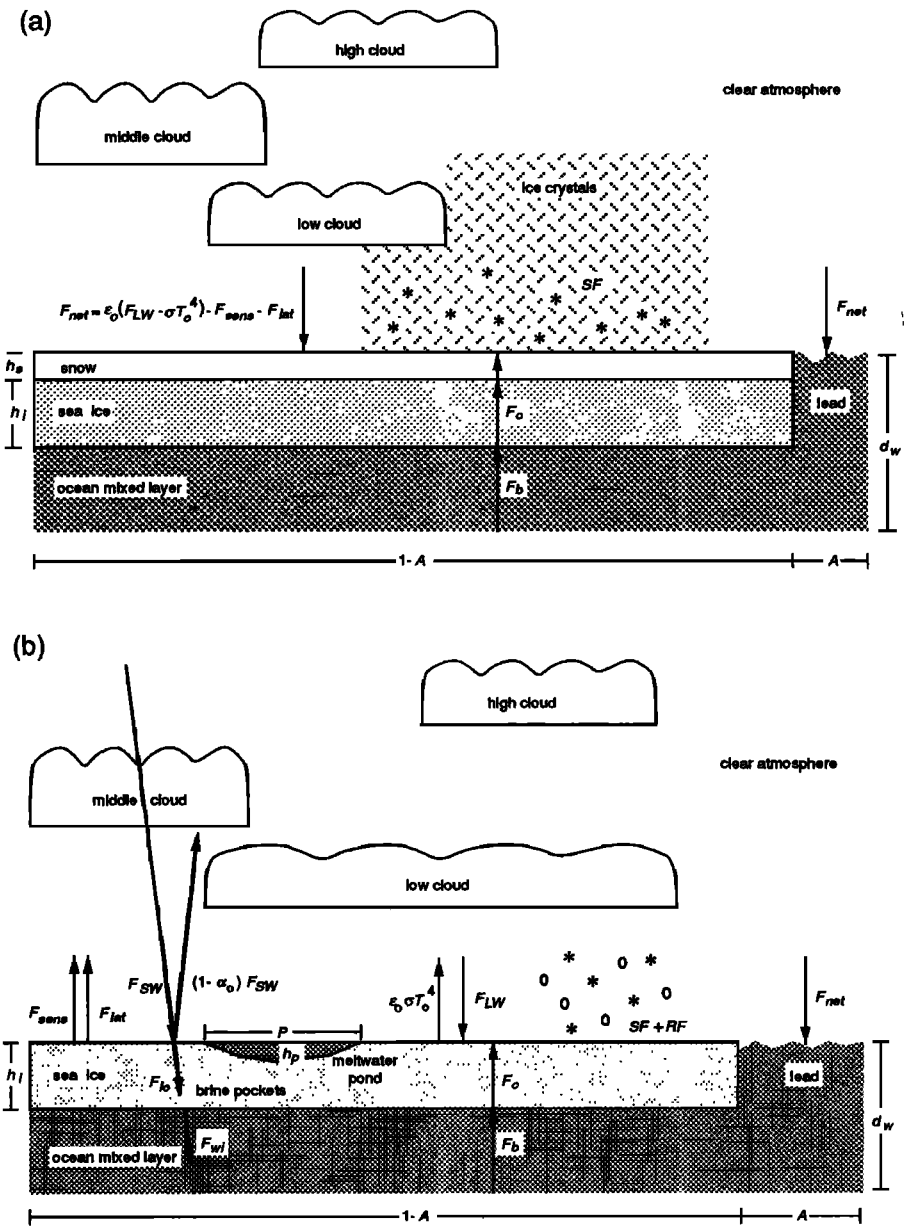

Fig. 1. Configuration of the one-dimensional model during (*a*) winter, and (*b*) summer.

In the absence of melting, the net flux at the upper surface of the ice, $(F_{net})_0$, must balance the conductive flux at the surface, $(F_c)_0$:

$$(F_{net})_0 \equiv \varepsilon_i (F_{LW} - \sigma T_0^4) + (1-\alpha_i)(1-I_0)F_{SW} - F_{sens} - F_{lat} = -(F_c)_0 \quad (2)$$

The surface temperature T_0 is determined by solving this flux balance equation. F_{LW} and F_{SW} are the fluxes of downward atmospheric longwave and shortwave radiation, and F_{sens} and F_{lat} are the fluxes of upward turbulent sensible and latent heat, respectively. The terms α_i and ε_i are the shortwave albedo and longwave emissivity of bare sea ice, respectively. I_0 is the fraction of the net absorbed solar radiation penetrating into the interior of the ice to form brine pockets when the surface is snow-free.

When the ice is covered by snow, a similar surface flux balance condition applies in the absence of melting:

$$(F_{net})_0 \equiv \varepsilon_s (F_{LW} - \sigma T_0^4) + (1-\alpha_s)F_{SW} - F_{sens} - F_{lat} = -(F_c)_0 \quad (3)$$

The surface temperature is determined by solving (3), where α_s and ε_s are the shortwave albedo and longwave emissivity of snow, respectively. The heat equation governs the conductive flux through the snow layer:

$$(\rho c)_s \frac{\partial T_s}{\partial t} = k_s \frac{\partial^2 T_s}{\partial z^2} = \frac{\partial F_c}{\partial z} \quad (4)$$

An internal snow temperature is computed to allow for storage of heat in the snow layer. The conductive flux between the ice and snow must be continuous, which couples equations (1) and (4) at the ice-snow interface.

For a melting snow or ice surface, the surface temperature is constrained not to exceed the melting point (273.15 K for snow, 273.05 K for ice). The resulting imbalance in (2) or (3) causes melting according to

$$\frac{\partial h_s}{\partial t} = \frac{-(F_{net})_0 - (F_c)_0}{L_{fs}} \qquad h_s \geq 0 \quad (5)$$

$$\left(\frac{\partial h_i}{\partial t}\right)_0 = \frac{-(F_{net})_0 - (F_c)_0}{L_{fi}} \qquad h_s = 0 \tag{6}$$

where L_{fs} and L_{fi} are the volumetric heats of fusion of snow and sea ice. An analogous equation applies to melting or accretion at the lower surface of the ice:

$$\left(\frac{\partial h_i}{\partial t}\right)_b = \frac{(F_c)_b - F_b}{L_{fb}} \tag{7}$$

where F_b is the heat flux from the ocean mixed layer beneath the ice. The latent heat of fusion at the bottom of the ice slab, L_{fb}, is slightly smaller than L_{fi} because a larger amount of brine is initially retained [*Schwarzacher*, 1959].

Throughout the year there is ongoing export of sea ice from the Arctic Basin. This can be expressed as

$$\partial A / \partial t = (1-A)\, D \tag{8}$$

where A is the lead fraction. The ice divergence D is prescribed to be a constant value of 4.5×10^{-9} s^{-1}, based on drifting buoy analyses in the central Arctic [*Colony and Thorndike*, 1984; *Mellor and Kantha*, 1989]. This corresponds to a transport of roughly 14% of the sea ice volume per year, in agreement with the observed range of ice export of 10-20% per year through Fram Strait [*Koerner*, 1973; *Vinje and Finnekasa*, 1986; *Moritz*, 1988].

2.2. *Brine Pockets and Snow and Ice Thermal Properties*

During the summer, when the ice surface is snow-free, solar radiation penetrates into the ice interior. This radiation warms the ice, soon forming pockets of brine in which latent heat is stored. The brine pockets retard internal temperature changes in either direction, but the overall effect is to increase the ice thickness over that determined for no penetrating solar radiation [*Maykut*, 1986].

Beer's law describes the flux of penetrating solar radiation, F_{i0}:

$$F_{i0}(z) = I_0(1-\alpha_i)F_{SW}e^{-\kappa_i z} \tag{9}$$

where α_i is the ice albedo and κ_i is the bulk shortwave extinction coefficient of sea ice. The temperature change in the ice follows the heat equation (1), with F_c replaced by F_{i0}. I_0, the fraction of penetrating solar radiation, is much smaller under clear skies (0.18) than under cloudy skies (0.35) [*Grenfell and Maykut*, 1977]; the effective value is obtained as

$$I_0 = 0.18\,(1-N) + 0.35\,N \tag{10}$$

where N is the fractional cloud amount.

The brine pockets may be parameterized explicitly [e.g., *Semtner*, 1976], or implicitly [e.g., *Untersteiner*, 1961; MU; *Ono*, 1967]. The implicit approach accounts for the effects of brine pockets by representing the bulk thermal conductivity k_i and volumetric heat capacity $(\rho c)_i$ of sea ice as functions of temperature and salinity. We follow MU in approximating these variations as

$$k_i = k_{if} + \frac{\beta S}{T_i - 273} \tag{11}$$

$$(\rho c)_i = (\rho c)_{if} + \frac{\gamma S}{(T_i - 273)^2} \tag{12}$$

The pure sea ice values are given by k_{if} and $(\rho c)_{if}$, and the constants, γ and β, have the values, $\gamma = 1.715 \times 10^7$ J K m^{-3} ppt^{-1} and $\beta = 0.1172$ W m^{-1} ppt^{-1}. To avoid a singularity at $T_i = 273$ K, MU constrained T_i not to exceed 272.9 K. We parameterize the salinity S of the sea ice to be a vertically constant function of ice thickness. For thin ice ($h_i < 0.6$ m), we use the approx-imation of *Cox and Weeks* [1974] for the average salinity of new ice. For thicker sea ice, a smaller value of $S = S_i = 3.2$ ppt is prescribed, representing the flushing effects of meltwater drainage through the ice over at least one melt season [*Weeks and Ackley*, 1986]:

$$\begin{aligned} S &= 14.24 - 19.39\, h_i \qquad & h_i &< 0.57 \text{ m} \\ S &= 3.2 & h_i &\geq 0.57 \text{ m} \end{aligned} \tag{13}$$

In the above expression h_i is in meters, and S is in parts per thousand.

The thermal conductivity of snow is a function primarily of its density. Many observational studies have led to expressions relating k_s to ρ_s. Following MU, we start with the formula of *Abels* [1892], which is representative of the median variation [see *Yen*, 1969]:

$$(k_s)_{thermal} = 2.845 \times 10^6\, \rho_s^2 \tag{14}$$

for k_s in watts per meter per degree and ρ_s in kilograms per meter cubed. In addition to direct conduction, the transfer of heat through snow is augmented by the process of water vapor diffusion, whereby vapor sublimes from the colder crystals and diffuses toward the warmer crystals [*Yen*, 1969; *Anderson*, 1976]. This transfer of latent heat increases the effective conduction by as much as 25% for the range of snow temperatures and densities observed in the Arctic. *Anderson* [1976] represented the increase in conductivity due to vapor diffusion as

$$(k_s)_{vap.diff.} = L_s\, D_e \frac{\partial q_s}{\partial T} \tag{15}$$

where $\partial q_s / \partial T$ is the variation of saturation specific humidity with temperature (computed as a function of temperature from the Clausius-Clapeyron equation) and D_e is the effective vapor diffusion coefficient, parameterized as

$$D_e = 9 \times 10^{-5} \left(\frac{T_s}{273}\right)^{14} \tag{16}$$

(units of meters squared per second). The right side of (16) can be represented as an exponential function of temperature with little loss of accuracy, resulting in an expression for snow conductivity that accounts for both direct thermal conduction and water vapor diffusion:

$$k_s = 2.845 \times 10^{-6}\, \rho_s^2 + 2.7 \times 10^{-4} \times 2^{(T_s - 233)/5} \tag{17}$$

Following *Anderson* [1976], the volumetric heat capacity of snow $(\rho c)_s$ is represented as a linear function of temperature,

$$(\rho c)_s = \rho_s\,(92.88 + 7.364\, T_s) \tag{18}$$

2.3. *Meltwater Ponds*

During the summer, when the surface is in a state of melting, a portion of the meltwater collects in ponds on the surface while the remainder runs off through cracks in the ice. Rainfall and snow also add to the water in the ponds. Because these ponds have a lower albedo than the bare ice, they decrease the aerially averaged albedo and increase the total amount of solar radiation absorbed at the surface. When the ponds refreeze in autumn they return latent heat to

the system, retarding cooling in a manner similar to that of the brine pockets [*Maykut*, 1986].

We introduce a parameterization which allows for a variable pond area P and depth h_p. Observations indicate that melt ponds form about 10 days after the onset of snow melt and increase rapidly in area, followed by a slow decrease in areal coverage due to drainage [*Nazintsev*, 1964] (cited by *Barry* [1989]). For simplicity we parameterize the pond fraction as a linear function of the time since the start of bare ice melting, having its maximum value at the start of the ice melt season, decreasing to a minimum value after 1 month, and remaining constant at that value until freeze-up. Maximum and minimum pond fractions, P_{max} and P_{min}, are chosen to be 0.25 and 0.10, respectively [*Nazintsev*, 1964; *Maykut*, 1986].

A prescribed fraction, f_{RO}, of surface meltwater is allowed to drain away while the rest accumulates in meltwater ponds. This runoff fraction is a highly uncertain quantity as it is difficult to measure, although it is thought that at least half of the meltwater drains off the surface [MU]. We tentatively set f_{RO} to 0.85, based on results of sensitivity experiments described in Section 4. We note that most sea ice models drain away all of the meltwater. *Mellor and Kantha*'s [1989] model allows for a layer of standing water on the ice surface, but does not adjust the surface albedo.

Meltwater increases owing to melting at the bare ice surface as described earlier, and also to melting at the bottom of the pond as a result of penetrating solar radiation which is absorbed both by the pond water and the underlying sea ice. This flux can be expressed by

$$F_p = F_{SW}\,[a_p + a_p\alpha_i t_p + t_p(1-\alpha_i)(1-I_0)] \qquad (19)$$

The first and second terms describe the solar radiation absorbed by the pond water, both directly and following reflection from the underlying ice. We assume that the albedo of the ice beneath the water can be approximated by the bare ice value. The third term represents the absorption of solar radiation by the ice below the pond. The pond transmissivity t_p can be approximated as a function of depth based on the transmission data given by *Neumann and Pierson* [1966]: $t_p = 0.36 - 0.17 \log_{10}(h_p)$. The ratio of absorption to extinction has a value of 0.89 for pure water [*Neumann and Pierson*, 1966], allowing the absorption coefficient to be calculated as $a_p = 1 - t_p^{0.89}$.

The pond depth is then calculated as

$$\frac{\partial h_p}{\partial t} = \left\{(1-P)\left(\frac{\partial h_i}{\partial t}\right)_0 + P\frac{F_p}{L_{fi}} + RF + SF\frac{\rho_s}{\rho_w}\right\}(1-f_{RO}) \qquad (20)$$

If h_p exceeds the maximum allowable depth, h_{pmax}, then it is set to h_{pmax} and the extra meltwater is added to the runoff. We adopt a value of 0.80 m for h_{pmax}, based on observations of *Chukanin* [1954] (cited by *Barry* [1989]).

At the end of the melt season, freezing occurs at the top of the ponds, and the melted water beneath the surface ice acts as a latent heat reservoir in the same manner as the brine pockets. The amount of latent heat added to the upper layer of the sea ice is $H_p = P\,h_p\,L_{fi}$.

2.4. *Leads*

The leads influence the energy balance of the sea ice by greatly increasing the upward turbulent flux of sensible and latent heat into the atmosphere during winter and enhancing the absorption of solar radiation during summer. The lead parameterization is adapted from that of *Parkinson and Washington* [1979] and accounts for a fraction A of leads with water temperature T_w. The expression for the net flux at the surface of the lead is similar to that for ice:

$$F_{aw} = \varepsilon_w F_{LW} - \varepsilon_w \sigma T_w^4 + (1-\alpha_w)(1-i_w)F_{SW} - F_{sens} - F_{lat} \qquad (21)$$

where ε_w is the emissivity of the water surface.

Maykut and Perovich [1987] showed that the solar flux through the lead is an important source of energy for warming the water adjacent to and below the sea ice. On the basis of measurements from the Arctic ice pack, they found that the fraction, $(1-i_w)$, of solar radiation absorbed by the water between the surface and depth h_i can be approximated as

$$(1-\alpha_w)(1-i_w) = a_1 + a_2 \ln h_i \qquad (22)$$

where a_1 and a_2 are constants ($a_1 = 0.5676$, $a_2 = 0.1046$ for clear skies, and $a_1 = 0.3938$, $a_2 = 0.1208$ for cloudy skies). This energy is used for lateral melting of the ice slab. The remainder of the absorbed solar flux, $(1-\alpha_w)i_w F_{SW}$, warms the water beneath the ice and contributes to ablation at the bottom of the ice.

When the surface net flux is positive, all of this energy is assumed to contribute to lateral melting of the sea ice slab:

$$\frac{\partial A}{\partial t} = \frac{A\,F_{aw}}{L_{fi}h_i + L_{fs}h_s} \qquad (23)$$

This simplification leads to a slight overestimation of the lateral ablation, since none of the energy is permitted to raise the temperature of the water next to the ice. However, the effect is small for small values of lead fraction [*Maykut and Perovich*, 1987].

The solar energy absorbed beneath the ice slab is the sum of the flux through the leads and the portion transmitted through the snow-free ice:

$$F_{wi} = A\,(1-\alpha_w)\,i_w\,F_{SW} + (1-A)\,(1-\alpha_i)I_0\,e^{-\kappa h_i}F_{SW} \qquad (24)$$

An additional source of energy to the ocean mixed layer is the vertical heat flux from the deeper ocean, F_{ocean}. The spatial distribution of ocean heat flux varies significantly in the Arctic, depending on the prevailing advection patterns [e.g., *Aagaard and Greisman*, 1975]. Measurements from the central Arctic suggest that F_{ocean} is negligible [*McPhee and Untersteiner*, 1982]; we therefore set $F_{ocean} = 0$. The temperature of the water beneath the ice, T_{wi}, is changed according to

$$\frac{\partial T_{wi}}{\partial t} = \frac{F_{wi} + F_{ocean} - (1-A)F_b}{[d_w - (\rho_i/\rho_w)h_i](\rho c)_w} \qquad (25)$$

where d_w is the depth of the ocean mixed layer, prescribed to be 30 m [*Lemke and Manley*, 1984], and $(\rho c)_w$ is the volumetric heat capacity of water. The heat flux at the base of the ice, F_b, represents the heat transfer due to molecular diffusion and turbulence, and leads to accretion or ablation at the base of the ice slab according to (7). F_b is computed as

$$F_b = (\rho c)_w C_{Tb}\,(T_{wi} - T_b)\,. \qquad (26)$$

The temperature of the bottom of the ice, T_b, is fixed at 271.2 K, the freezing point of sea water. Our method for relating T_{wi} and F_b is similar to *Harvey*'s [1990] "Method 5" for computing basal heat flux, which produced realistic heat fluxes in the Arctic.

Mellor and Kantha [1989] describe a complex method for computing the bulk transfer coefficient C_{Tb} which can be approximated as

$$C_{Tb} = \frac{u_\tau^{1/2}}{4100\,b\,z_{0i}^{1/2}} \qquad (27)$$

In this expression, u_τ is the friction velocity, z_{0i} is the roughness length at the bottom of the ice (set to 0.05 m for $h_i \geq 3$m, decreasing linearly to zero for $h_i = 0$), and b is a parameter. Using values of $u_\tau = 0.01$ m s^{-1} [*Kantha and Mellor*, 1989] and $b = 1.5$ [*Mellor and Kantha*, 1989], we arrive at the following expression for C_{Tb}:

$$C_{Tb} = 1.26 \times 10^{-4} h_i^{-1/2} \qquad h_i < 3 \text{ m}$$
$$C_{Tb} = 7.27 \times 10^{-5} \qquad h_i \geq 3 \text{ m} \tag{28}$$

If F_{aw} is negative, then water is frozen laterally onto the ice slab, reducing the lead fraction according to (23). The lead fraction is constrained not to fall below a minimum value A_{min} prescribed to be 0.005. A_{min} parameterizes the continual opening of leads in winter due to wind and ocean stresses on the ice and has been used in other sea ice models [e.g., *Parkinson and Washington*, 1979; *Shine and Crane*, 1984; *Ledley*, 1987]. If A falls below A_{min}, it is reset to the value of A_{min} and the excess ice is added to the depth of the slab, representing ridging. The ocean temperature is not allowed to fall below 271.2 K. Further cooling of the water beneath the ice results in accretion of ice onto the bottom of the slab.

At the end of the time step, the water in the lead is mixed with the water beneath the ice.

2.5. *Atmospheric Turbulent Fluxes*

The turbulent processes interact with the overlying atmosphere through the surface temperature, lead fraction, and state of melting. Climatological values of atmospheric temperature T_a and moisture q_a were taken from *Oort* [1983] for 80°N at 1000 hPa and are given in Table 1. Daily values were obtained by a cubic spline interpolation through the monthly mean values. A constant surface wind speed u_a of 5 m s^{-1} is prescribed [*Vowinckel and Orvig*, 1970].

At the surface the turbulent heat and moisture fluxes are parameterized using bulk aerodynamic formulae,

$$F_{sens} = \rho_a c_p C_T u_a (T_0 - T_a) \tag{29a}$$

$$F_{lat} = \rho_a L_v C_T u_a (q_{sat}(T_0) - q_a) \tag{29b}$$

over sea ice and

$$F_{sens} = \rho_a c_p C_T u_a (T_w - T_a) \tag{30a}$$

$$F_{lat} = \rho_a L_v C_T u_a (q_{sat}(T_w) - q_a) \tag{30b}$$

over water, where $q_{sat}(T)$ refers to the saturation specific humidity. Although the bulk formulae do not explicitly model the intermittent turbulence that may occur in the very stable wintertime atmospheric boundary layer, its effects may be approximated by using a stability-dependent transfer coefficient, C_T. We compute C_T as a decreasing function of increasing atmospheric stability following *Louis* [1979]:

$$C_T = C_{T0}\left(1 - \frac{2\,b'\,Ri}{1 + c\,|Ri|^{1/2}}\right) \qquad Ri < 0$$
$$C_T = C_{T0}(1 + b'\,Ri)^{-2} \qquad Ri \geq 0 \tag{31}$$

where Ri is the bulk Richardson number,

$$Ri = \frac{g\,(T_a - T_0)\,\Delta z}{T_a\,u_a^2}$$

for a height Δz of 10 m. The Richardson number is calculated separately over ice and open water. The parameter c has a value of (1961 $b'\,C_{T0}$) for a roughness length of 1.6×10^{-4} m over ice [*Leavitt et al.*, 1978], and b' is a parameter used in fitting Louis' parameterization to Businger's flux-profile formulae (see *Louis* [1979] for details). Louis uses a value of $b' = 4.7$, but this value leads to a large overestimate of the downward heat flux in stable conditions (see Louis' Figure 2*a*). We find that a larger value, $b' = 20$, provides good agreement between Businger's formulae and Louis' parameterization for $Ri \geq 0$, while producing no significant change in the parameterization for $Ri < 0$. C_{T0} is a transfer coefficient for the neutral surface layer, assumed to be equal for heat and moisture and assigned a value of 1.3×10^{-3} for ice [*Andreas*, 1987] and 1.0×10^{-3} for leads [*Andreas and Murphy*, 1986].

2.6. *Precipitation*

The prescribed precipitation, given in Table 1, is derived from climatological data for stationary and drifting stations in the vicinity of 80°N [*Vowinckel and Orvig*, 1970]. The climatological values were multiplied by a factor of 1.6, as it is known that gauge measurements underestimate winter snowfall by at least 60% since many trace readings are recorded as zero [*Barry*, 1989]. Daily values were obtained by a cubic spline interpolation through the monthly mean values. Approximately one tenth of the summertime precipitation falls as rain. Unlike the MU model, the snowfall is not "turned off" during the melt season, but is allowed to fall and melt

TABLE 1. Mid-Monthly Values of Forcing Variables

Forcing Variable	Jan.	Feb.	March	April	May	June	July	Aug.	Sept.	Oct.	Nov.	Dec.	Source
T_a, K	248.7	247.8	248.8	253.4	263.5	271.1	274.3	273.3	268.5	261.2	255.4	251.7	*Oort* [1983]
q_a, g kg^{-1}	0.4	0.4	0.4	0.6	1.5	2.8	3.6	3.6	2.6	1.6	0.7	0.6	*Oort* [1983]
u_a, m s^{-1}	5	5	5	5	5	5	5	5	5	5	5	5	*Vowinckel and Orvig* [1970]
RF, mm d^{-1} x 10^2	0	0	0	0	0	1.2	5.1	6.2	1.0	0	0	0	*Vowinckel and Orvig* [1970]
SF, mm d^{-1} x 10^2	80.8	87.2	66.9	78.4	110.1	177.3	1.9	2.2	2.6	2.2	1.2	84.0	*Vowinckel and Orvig* [1970]
F_{ocean}, W m^{-2}	0	0	0	0	0	0	0	0	0	0	0	0	*McPhee and Untersteiner* [1982]
N	0.81	0.78	0.81	0.71	0.78	0.83	0.85	0.87	0.85	0.89	0.78	0.78	*Curry and Ebert* [1992]
Radiative Forcing Variable	Jan.	Feb.	March	April	May	June	July	Aug.	Sept.	Oct.	Nov.	Dec.	
F_{LW}, W m^{-2}	168.3	167.2	171.8	178.5	221.2	271.5	290.9	287.1	249.6	211.8	186.8	176.0	
F_{SW}, W m^{-2}	0.0	0.0	20.5	138.4	281.0	328.1	235.6	142.4	51.0	1.7	0.0	0.0	
Direct/diffuse	0.284	0.284	0.519	1.044	0.721	0.381	0.432	0.398	0.395	0.266	0.284	0.284	
w_1	0.520	0.520	0.503	0.492	0.504	0.527	0.545	0.539	0.517	0.519	0.520	0.520	
w_2	0.343	0.343	0.343	0.339	0.338	0.340	0.315	0.321	0.339	0.343	0.343	0.343	
w_3	0.129	0.129	0.142	0.153	0.144	0.124	0.130	0.130	0.134	0.130	0.129	0.129	
w_4	0.008	0.008	0.012	0.016	0.014	0.009	0.010	0.010	0.010	0.008	0.008	0.008	

The radiative forcing variables were computed for the baseline case. These values were then prescribed in the sensitivity experiments.

upon contact with the melting surface, assuming a summertime snow density of 450 kg m^{-3} [*Loshchilov*, 1964]. As is described in section 2.3, a fraction of the rain or melted snow is allowed to run off, while the remainder accumulates in melt ponds.

2.7. *Surface Albedo*

We devote particular attention to the parameterization of the surface albedo so that the sea ice model can be coupled to a detailed radiation model and the radiative feedbacks between the atmosphere and sea ice can be elucidated.

Clouds influence the surface albedo by selectively absorbing solar radiation at wavelengths greater than about 0.7 μm. Because the spectral reflectivies of snow and ice are greater in the visible region than in the near-infrared, the surface albedo under clouds exceeds the clear-sky value. This has been clearly demonstrated by measurements [e.g., *Grenfell and Maykut*, 1977; *Grenfell and Perovich*, 1984] and modeling studies [e.g., *Choudhury and Chang*, 1981; *Shine and Henderson-Sellers*, 1985]. In addition, clouds alter the distribution of the solar flux between direct and diffuse components. This can be important for surface types whose reflection characteristics are not Lambertian. In particular, the direct albedos of dry snow and open water depend significantly on the angle of the Sun [*Wiscombe and Warren*, 1980; *Briegleb et al.*, 1986].

Our surface albedo parameterization considers both the spectral variation in albedo as well as its dependence on solar zenith angle. Five surface types are included: new snow, melting snow, bare ice, meltwater ponds, and open water. We partition the solar spectrum into four intervals, following *Curry and Ebert* [1992]: (1) 0.25 - 0.69 μm, (2) 0.69 - 1.19 μm, (3) 1.19 - 2.38 μm, and (4) 2.38 - 4.00 μm. The integrated surface albedo is the sum of the spectral albedos weighted by the relative solar flux, w_j, in each wavelength region, i.e.,

$$\alpha = \sum_{j=1}^{4} w_j \alpha_j$$

and further weighted by the direct and diffuse fractions, f_{SWdir} and f_{SWdif}, respectively. Table 2 summarizes the spectral albedos for the five surface types considered in the model. The weights are discussed later in this section. The albedo parameterizations for the first four surface types are shown in Figure 2, along with the data from which they were derived.

The direct albedo of dry snow (Figure 2*a*) is a function of the solar zenith angle, θ_0, and is approximated from a linear least squares fit to the model results of *Wiscombe and Warren* [1980]. It has a maximum spectrally integrated value of 0.82 at $\theta_0 = 90°$, decreasing to a value of 0.76 for $\theta_0 = 50°$. The diffuse albedo of dry snow (Figure 2*b*) is derived from the observations of *Grenfell and Perovich* [1984], who measured spectral albedos in the range 0.4-2.4 μm for various surface characteristics on the sea ice near Point Barrow, Alaska. The diffuse albedo in band 4 is from *Shine and Henderson-Sellers* [1985]. Because only a thin layer of snow is required to achieve a relatively large optical thickness, the dependence of snow albedo on depth is negligible for h_s greater than about 0.1 m. Following *Shine and Henderson-Sellers* [1985], we assume that the albedo of a thin layer of snow ($h_s < 0.1$ m) decreases linearly toward the bare ice value.

The diffuse albedo of melting snow (Figure 2*b*) is less than that for dry snow owing to increased grain size. Again, the spectral values are taken from the measurements of *Grenfell and Perovich* [1984] for bands 1-3 and *Shine and Henderson-Sellers* [1985] for band 4. The diffuse albedo of bare sea ice is a function of its age, as the brine and bubble volumes change during the melt season, and thickness, as the dark ocean surface beneath the slab increasingly influences the shortwave absorption for thinner ice. Figure 2*c* shows the spectral distribution of ice albedo used in the albedo parameterization. We assume that the age and thickness of the sea ice are correlated, so that small h_i corresponds to first-year ice and larger h_i corresponds to multiyear ice. For sea ice less than 1 meter thick, logarithmic curves were fit to the model results of *Grenfell* [1983], relating young ice albedo to ice thickness. For $1.0 \le h_i \le 2.0$ m, the ice albedo is linearly interpolated between the *Grenfell* [1983] values at 1.0 m and the spectral measurements of *Grenfell and Maykut* [1977] for multiyear ice. The *Grenfell and Maykut* [1977] values are adopted for $h_i \ge 2.0$ m, since the albedo is nearly independent of ice thickness for thick multiyear ice.

TABLE 2. Spectral Albedos for Five Surface Types

Surface Type	Band 1 0.25 - 0.69 μm	Band 2 0.69 - 1.19 μm	Band 3 1.19 - 2.38 μm	Band 4 2.38 - 4.00 μm
Dry snow, α_s				
Direct	0.980-0.008 μ_0	0.902-0.116 μ_0	0.384-0.222 μ_0	0.053-0.047 μ_0
Diffuse	0.975	0.832	0.250	0.025
Melting snow, α_s				
$h_s \ge 0.1$ m	0.871	0.702	0.079	0.010
$h_s < 0.1$ m	linearly reduced to bare sea ice value	linearly reduced to bare sea ice value	linearly reduced to bare sea ice value	linearly reduced to bare sea ice value
Bare sea ice, α_i				
$h_i < 1$ m	0.760+0.140 ln h_i	0.247+0.029 ln h_i	0.055	0.036
$1 \le h_i < 2$ m	0.770+0.018 (h_i-1)	0.247+0.196 (h_i-1)	0.055	0.036
$h_i \ge 2$ m	0.778	0.443	0.055	0.036
Meltwater pond, α_p	0.150+exp(-8.1 h_p-0.47)	0.054+exp(-31.8 h_p-0.94)	0.033+exp(-2.6 h_p-3.82)	0.030
Open water, α_w				
Direct	α_w^*+0.008	α_w^*-0.007	α_w^*-0.007	α_w^*-0.007
Diffuse	0.060	0.060	0.060	0.060

Here, $\mu_0 = \cos\theta_0$ and $\alpha_w^* = 0.026 / (\mu_0^{1.7}+0.065) + 0.015\,(\mu_0-0.1)(\mu_0-0.5)(\mu_0-1.0)$.

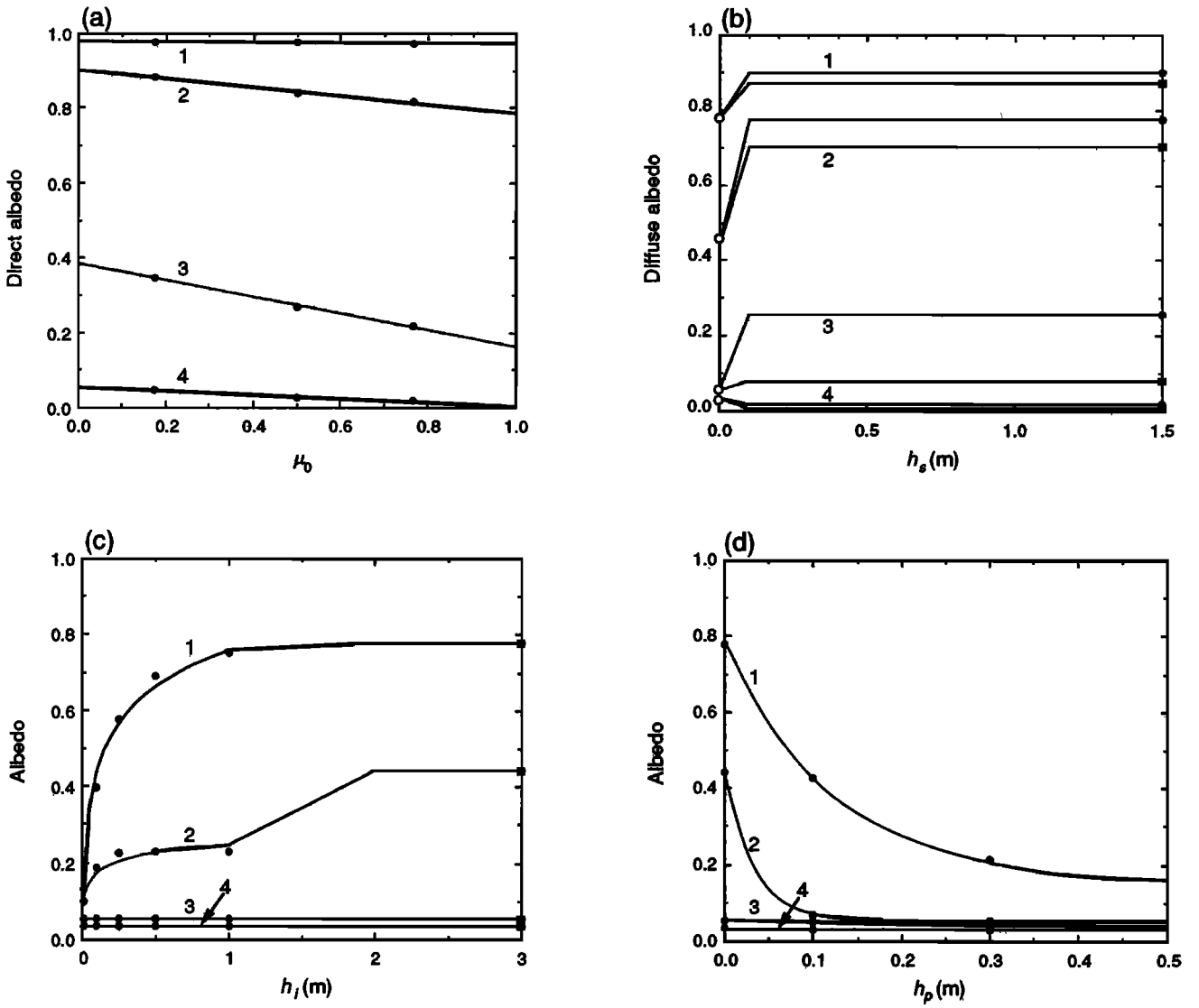

Fig. 2. Albedo parameterization (solid lines) in shortwave spectral bands 1-4 for four surface types. (*a*) Dry snow direct albedo; also shown are the model results of *Wiscombe and Warren* [1980] (solid circles). (*b*) Diffuse albedos of dry and melting snow; also shown are the observations of *Grenfell and Perovich* [1984] for dry (solid circles) and melting (solid squares) snow, and the observations of *Grenfell and Maykut* [1977] for bare multiyear ice (open circles). (*c*) Bare sea ice; also shown are the model results of *Grenfell* [1983] for young ice (solid circles) and observations of *Grenfell and Maykut* [1977] for multiyear ice (solid squares). (*d*) Melt pond; also shown are the combined observations of *Grenfell and Maykut* [1977] and *Grenfell and Perovich* [1984] (solid circles).

The albedo of a meltwater pond (Figure 2*d*) is significantly lower than that of bare ice and decreases with increasing pond depth, h_p. Few direct observations exist for individual melt ponds. We parameterize the dependence of the diffuse pond albedo on h_p from the observations of *Grenfell and Maykut* [1977] and *Grenfell and Perovich* [1984] using a decaying exponential function. The spectral albedo in band 4 is extrapolated from Grenfell and Perovich's values at 2.4 μm; since only about 1% of the summertime solar flux occurs in this band, this approximation leads to negligible error in the spectrally integrated albedo. The parameterization produces an integrated pond albedo of 0.26 for h_p = 0.1 m and 0.14 for h_p = 0.3 m.

The albedo of the ocean surface, α_w, depends strongly on the solar zenith angle, especially when winds are calm or light. The parameterization of *Briegleb et al.* [1986] is used here, yielding a spectrally integrated albedo of 0.05 at θ_0 = 50°, and 0.40 for specular reflection when the sun is on the horizon.

The zenith angle dependencies of the albedos of melting snow, bare ice, and meltwater ponds are less prevalent in the literature, and we have made no attempt to model or parameterize them. By doing this, we are implicitly assuming that the direct albedo is approximately equal to the diffuse albedo. Since these three surface types occur only in summer when the sky is nearly overcast, this approximation should introduce little error in the calculated overall albedo.

2.8. *Radiative Fluxes*

The daily fluxes of solar and longwave radiation for the baseline simulation were computed by coupling the sea ice model to a detailed cloud radiation model, after *Curry and Ebert* [1992]. We prescribe a variable fractional cloud cover N based on randomly overlapping layers of low, middle, and high clouds, whose respective thicknesses and amounts were taken from the "air-calibrated" statistics of *Huschke* [1969] for the central Arctic. We also include

a layer of wintertime low level ice crystal precipitation whose thickness and fractional coverage are dependent on the air temperature and humidity. The atmospheric and cloud temperatures are specified from *Oort*'s [1983] atmospheric temperature and humidity profiles at 80°N. Unfortunately, the annual cycle of atmospheric and cloud conditions is not well known in the Arctic, but the use of these prescribed values produces realistic downward longwave and shortwave fluxes, as noted below. Figure 3 shows the annual cycle of cloud distribution. The annual cycle of total cloud fraction is listed in Table 1.

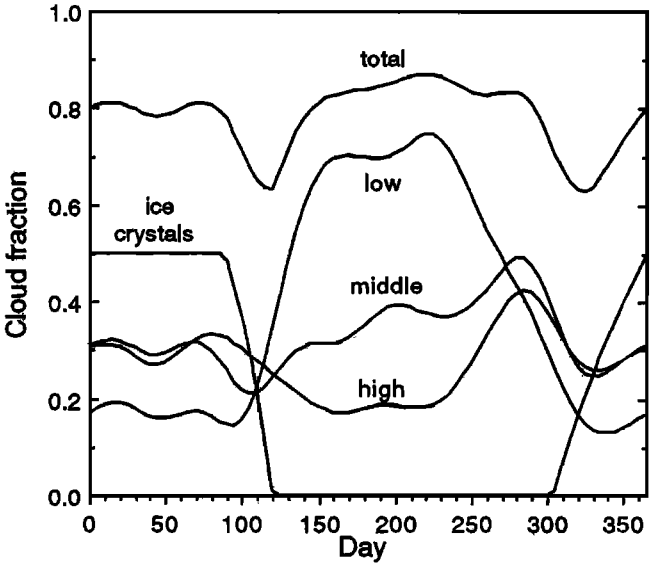

Fig. 3. Annual cycle of low, middle, high, low level ice crystal, and total cloudiness [after *Curry and Ebert*, 1992].

The shortwave radiative model is described in detail by *Ebert and Curry* [1992] and *Curry and Ebert* [1992] and will be briefly summarized here. It uses a two-stream algorithm [*Slingo*, 1989] to compute the direct and diffuse reflectivities and transmissivities of single cloud layers, using cloud droplet- and density-dependent optical properties based on *Slingo* [1989] for water clouds and *Takano and Liou* [1989] for ice clouds. The clear-sky fluxes are calculated using the *Lacis and Hansen* [1974] scheme. The multiple reflections between cloud layers and the surface are modeled after *Harshvardhan et al.* [1987].

The longwave radiative model is also detailed by *Ebert and Curry* [1992]. It is a five-band model which again employs cloud droplet- and density-dependent optical properties, this time based on *Curry and Herman* [1985] for water clouds, and parameterized from Mie calculations for ice clouds. The model estimates spectral emissivities, which are then used along with cloud temperatures to determine the integrated longwave flux from the clouds. The clear-sky fluxes are computed following *Curry and Herman* [1985].

3. ANNUAL CYCLE

In this section we present results from the equilibrium annual cycle of the sea ice model for the baseline case, that is, when the set of forcing variables in Table 1 is used to force the model. The intent in this section is to assess the ability of the one-dimensional model to reproduce normal multiyear sea ice conditions. Our model results are compared with observations and other calculations. An 11-day running mean filter was applied to the time series to smooth the effect of sudden changes in conditions (i.e. onset of melting, onset of snow accumulation) and simulate the smoothing which would result from averaging a spatially variable field.

3.1. *Snow and Ice Thickness*

The model's annual cycle of snow and ice thickness is shown in Figure 4. Also shown are *Untersteiner*'s [1961] multiyear sea ice thickness observations from International Geophysical Year (IGY, 1957-1958) station Alpha, *Maykut*'s [1982] average ice thickness from the Arctic Ice Dynamics Joint Experiment (AIDJEX) manned array, and numerical results from the MU model.

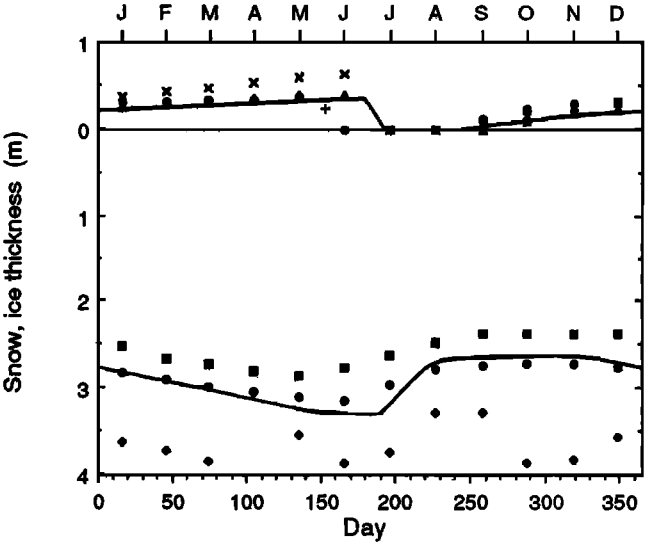

Fig. 4. Annual cycle of snow depth h_s and ice thickness h_i. Also shown are the observations of *Untersteiner* [1961] (solid squares) and *Maykut* [1982] (solid diamonds), and the model results of MU (solid circles) for sea ice thickness, and data presented by *Loschilov* [1964] (solid triangles), *Koerner* [1973] (pluses), *Ross and Walsh* [1987] (crosses), and MU's parameterization (solid circles) for snow depth.

Quantities describing the mass balance are compared in Table 3. The model's mean annual ice thickness of 2.89 m is in good agreement with the typical multiyear sea ice thickness of 3 m [e.g., *Koerner*, 1973; *Bourke and Garrett*, 1987]. The ice thickness h_i increases from a minimum value of 2.60 m in autumn to a maximum value of 3.26 m in mid-June, in qualitative agreement with observations. The yearly surface ice ablation and bottom accretion both slightly exceed the observed values for station Alpha. The annual bottom ablation of 0.10 m is slightly greater than that of MU but less than observed at station Alpha, and the annual surface runoff of 0.48 m is slightly greater than was observed at Station Alpha. When lateral ice growth and decay is included, the total ice accretion increases to 1.15 m and the total ice ablation (not including the water retained in melt ponds) is 0.74 m. This is balanced by 0.41 m (equivalent) of ice export. These values are in good agreement with Koerner's annual mass balance figures of 1.1 m for accretion, 0.6 m for ablation, and 0.5 m for export from the Arctic Basin.

Snow in the model begins accumulating at the end of August, continuing until the start of ablation season in the end of June. The snow thickness h_s is in good agreement with the observed values of *Loshchilov* [1964], *Koerner*'s [1973] observations from the British Trans-Arctic Expedition (1968-1969), and parameterized values of MU but smaller than the calculated snowfall of *Ross and Walsh* [1987]. The prescribed annual snowfall is greater than that used by MU (Table 3). However, much of the snow falls in summer and melts upon contact with the warm surface, and thus does not contribute to snow accumulation. The onset of snow melt is almost 3 weeks later in the model than in the MU simulation and the observations from station Alpha but still within the range of interannual variability reported by *Robinson et al.* [1987].

TABLE 3. Mass Balance

	Model	MU	IGY Station Alpha [*Untersteiner*, 1961]
Mean ice thickness, m	2.89	2.88	2.57
Surface ice ablation, m	0.57	0.40	0.44
Runoff, m	0.48	0.40	0.34
Water retained in ponds, m	0.09	0.00	0.10
Bottom ice ablation, m	0.10	0.05	0.26
Bottom ice accumulation, m	0.66	0.45	0.63
Accretion, m	0.66	0.45	0.63
Ridging, m	0.00	0.00	0.00
Lateral ice ablation, m equivalent	0.16	0.00	
Lateral ice accretion, m equivalent	0.49	0.00	
Ice export, m equivalent	0.41	0.00	
Snow accumulation, m snow	0.39	0.40	0.38
Total snowfall, m snow	0.52	0.40	0.38
Total rainfall, m water	4×10^{-3}	0.00	0.00
Onset of snow ablation, day	178	159	156
Onset of ice surface ablation, day	191	180	180
End of ice surface ablation, day	232	231	221
Onset of ice bottom ablation, day	176	198	162
End of ice bottom ablation, day	299	308	312

3.2. *Surface Temperature*

The sea ice surface temperature in the model, T_0, (Figure 5) has a minimum value of 239.6 K in mid-February, increasing to the melting temperature of snow, 273.15 K, in late June. Except for a phase shift of a few weeks, there is good agreement between the predicted ice surface temperature and available observations [*Banks and Partanen*, 1959; *Maykut*, 1978]. The modeled surface temperature is somewhat cooler than the observed values in spring. As will be seen later, this is due primarily to the use of a stability-dependent atmospheric turbulent flux parameterization, which produces a cold season sensible heat flux which is smaller than other calculated values, and a deficit in the modeled net longwave flux at the surface. T_0 is warmer than observed in the fall as a result of a large conductive flux from the ocean mixed layer due to solar heating in the leads. We note that observations from drifting stations, which are located on thicker ice, have smaller conductive fluxes than are found in the surrounding pack ice [*Koenig et al.*, 1952].

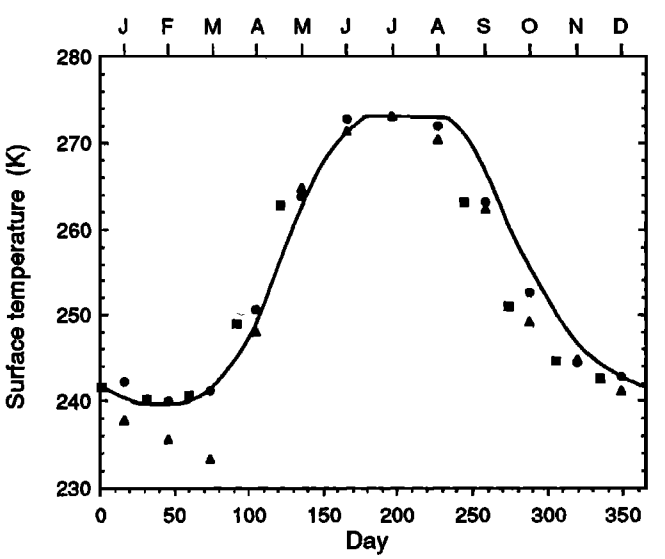

Fig. 5. Annual cycle of sea ice surface temperature T_0. Also shown are the observations of *Banks and Partanen* [1959] (solid triangles) and *Maykut* [1978] (solid squares), and the model results of MU (solid circles).

3.3. *Surface Albedo*

The annual cycle of spectrally integrated surface albedo, α_0, is shown in Figure 6, along with observations from Soviet drifting stations of *Nazintsev* [1964] and *Chernigovskii* [1968] and satellite observed surface albedo of *Scharfen et al.* [1987]. Our model produced a ponded ice albedo of 0.50, in agreement with *Nazintsev*'s [1964] observed albedos of roughly 0.50 over ponded ice on "North Pole" drifting stations. MU used prescribed albedos that were essentially the same as the *Chernigovskii* [1968] values, which are seen to be much higher than the other albedos in Figure 6. The lower surface albedo in the present calculation, compared with the prescribed values used by MU, accounts in large part for the difference in surface ablation between our results and theirs. The phase shift of roughly 3 weeks is due to the late onset of snow melt in early summer and the occurrence of the maximum lead extent in autumn (shown in section 3.7), which was not accounted for in the Soviet observations.

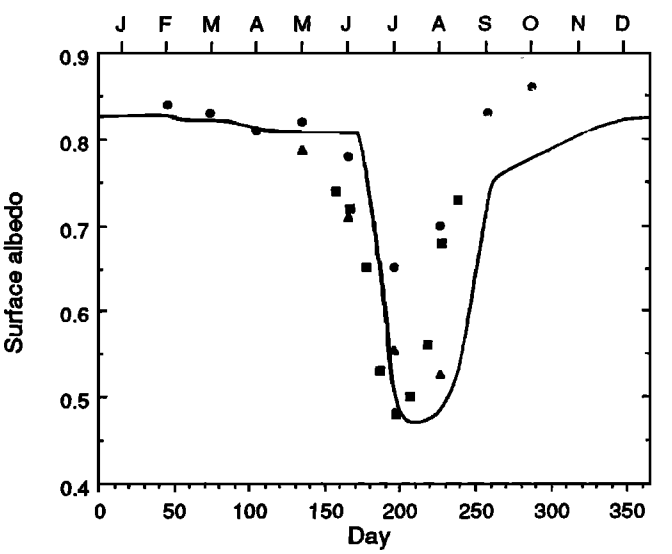

Fig. 6. Annual cycle of surface albedo α_0. Also shown are the observations of *Nazintsev* [1964] (solid squares), *Chernigovskii* [1968] (solid circles), and *Scharfen et al.* [1987] (solid triangles).

3.4. *Radiative Flux*

The downward longwave and shortwave fluxes for the baseline case are discussed in detail in *Curry and Ebert* [1992], and are not shown here. Mid-monthly values of F_{LW}, F_{SW}, ratio of direct/diffuse radiation for the integrated solar flux, and the spectral distribution (w_1-w_4) of the solar flux are shown in Table 1. The fluxes are in good agreement with observed monthly average downward fluxes of *Marshunova* [1961] and *Vowinckel and Orvig* [1970].

Figure 7 shows the net shortwave, $(1-\alpha_0)F_{SW}$, and longwave, $\varepsilon_0(F_{LW}-\sigma T_0^4)$, fluxes from the model, compared with the observations of *Makshtas* [1984] and the calculations of *Maykut* [1978, 1982, 1986] and MU. (In this figure the net shortwave flux includes the amount of radiation absorbed in the ice interior, $(1-\alpha_0)I_0F_{SW}$, in order to compare our results with other published values.) The net shortwave flux rises from March until the summer solstice, when it begins to gradually decline as the incoming flux

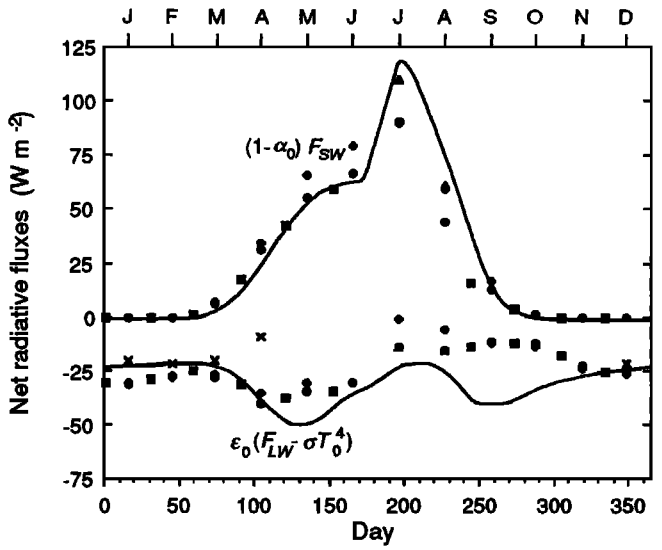

Fig. 7. Annual cycle of area-averaged net shortwave and longwave fluxes. Also shown are the observations of *Makshtas* [1984] (crosses), as well as the calculations of *Maykut* [1978] for 3-m ice (solid squares), *Maykut* [1982] (solid diamonds), *Maykut* [1986] (solid triangles), and the model results of MU (solid circles).

TABLE 4. Energy Balance

Annual Total Energy, $\times 10^8$ J m^{-2}	Model	MU	AIDJEX [*Maykut*, 1982]
Downward solar radiation	31.86	31.55 *	31.55 *
Net solar radiation	9.30	7.62	9.32
Solar radiation penetrating into ice	2.08	0.54	0.95
Downward longwave radiation	67.91	69.45 *	69.45 *
Net longwave radiation	-8.96	-7.70	-7.04
Sensible heat	-0.58	-1.13 *	0.40
Latent heat	0.49	1.34 *	1.59
Net flux at surface	0.42	-0.29	0.29
Conductive flux at surface	2.56	2.51	3.95
Solar flux entering ocean beneath ice	0.51	0.01	1.07
Heat flux at base of ice	0.56	0.63 *	0.63 *

*Prescribed.

decreases. At the onset of snowmelt, however, the albedo drops rapidly and the net shortwave flux increases sharply as more radiation is absorbed by the surface. The peak value of 121 W m^{-2} is in good agreement with *Maykut* [1986], who adjusted the summertime results of MU to account for meltwater ponds. His correction resulted in a midsummer increase in net shortwave flux of 20 W m^{-2}, which has a strong effect on the equilibrium sea ice thickness as will be shown in section 4. The other two *Maykut* [1978, 1982] calculations did not account for melt ponds. The inclusion of leads adds a further increase of 4-7 W m^{-2} over the ice-only value to the area-averaged summertime net shortwave flux.

Table 4 shows the annual energy balance computed for the baseline case, compared with MU's model results and *Maykut*'s [1982] calculations from the AIDJEX data. The baseline annual net solar radiation is greater than the calculated value of MU, who modeled only multiyear ice with no leads, and close to the value of *Maykut* [1982], who used an ice thickness distribution with eight categories including open water.

The net longwave flux is negative throughout the year, with a minimum value of -50 W m^{-2} occurring in late spring. It is in reasonable agreement with the observations and calculations. The discrepancy in the autumn months results from the model's overestimate of the surface temperature (Figure 5); about 3 W m^{-2} of the deficit results from the inclusion of leads. As a result, the annual net longwave radiation is more negative than the values computed by MU and *Maykut* [1982].

3.5. *Atmospheric Turbulent Fluxes*

Figure 8*a* shows the sensible heat flux F_{sens} predicted by the model. Also included are the calculated sensible heat fluxes of *Doronin* [1963], *Badgley* [1966], *Leavitt et al.* [1978], *Maykut* [1978, 1982], and *Makshtas* [1984]. There is substantial variation in the calculated annual cycles, but in general they show negative, or downward, sensible heat fluxes in winter and positive fluxes in summer. Our modeled sensible heat flux shows the best agreement with that of *Leavitt et al.* [1978]. As was noted by *Maykut* [1986], the values of *Leavitt et al.* [1978] may be more accurate than the other monthly values shown in Figure 8*a* because they took atmospheric stability into account in their calculations. *Nikoforov et al.* [1990] point out that the neglect of atmospheric stability can result in the overestimation of turbulent heat and moisture fluxes by a factor of 2-3, especially during inversion conditions.

The modeled sensible heat flux (solid line) is an area-weighted average of the sensible heat fluxes over the ice (dashed line) and open water. In winter, the downward flux over ice (~ -5 W m^{-2}) is in part counterbalanced by the strong upward flux over the small area of open water (~ 250 W m^{-2}). In autumn the sensible heat flux over leads is smaller (~ 100 W m^{-2}) but the greater fractional area (section 3.7) gives it greater impact. The peaks in June and August, evident in both our model results and the other calculations, result from the constraint on the surface temperature not to exceed the melting point, while the air temperature has its maximum value in midsummer (Table 1). The annual average sensible heat flux is close to zero and is midway between the average values of MU and *Maykut* [1982] (Table 4).

The latent heat flux, F_{lat}, (Figure 8*b*) has values near zero in winter, due to the low moisture content of the cold air near the surface. The summertime values of F_{lat} are positive and of the same magnitude as the sensible heat flux, and show a similar multipeaked structure. Our modeled latent heat flux is somewhat larger in magnitude than the values of *Leavitt et al.* [1978] but smaller than the others shown in Figure 8*b* and listed in Table 4.

3.6. *Net Flux at the Surface*

The net flux F_{net} is the sum of the net shortwave, longwave, sensible, and latent heat fluxes. Figure 9*a* shows the area-averaged component terms and the total net flux (bold line), as well as the net flux calculated in three other studies. The net flux is dominated by the negative longwave component in winter and by the positive shortwave component in summer, while the turbulent fluxes play relatively minor roles. The predicted net flux is less negative than the calculations of *Maykut* [1978, 1982] and MU in winter, less positive in spring, and more negative in autumn, owing primarily to differences in the net longwave and sensible heat fluxes. However, the modeled annual mean net flux of +1.3 W m^{-2} is quite close to the annual mean values of -0.9 W m^{-2} for the MU thermodynamic model and +0.9 W m^{-2} for sea ice in the AIDJEX manned array [*Maykut*, 1982].

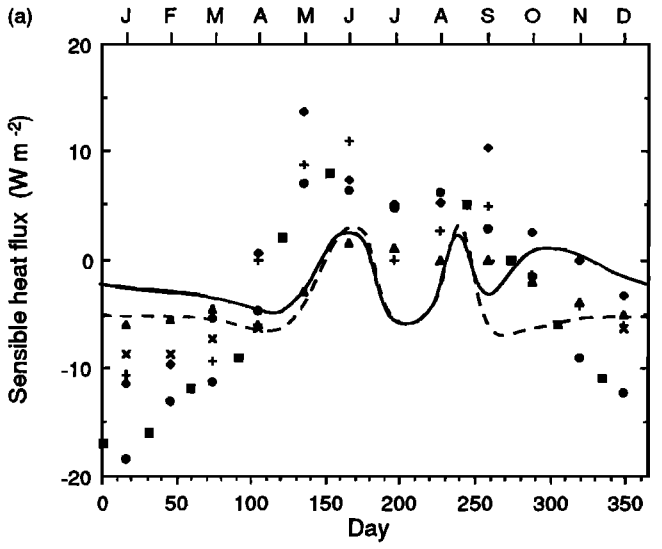

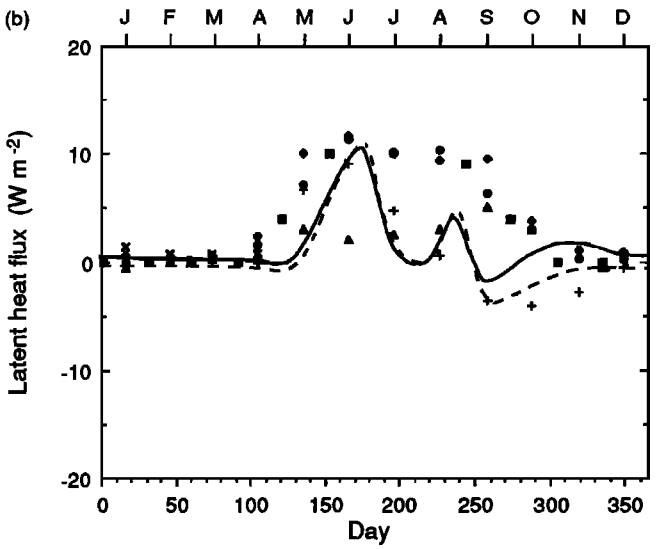

Fig. 8. Annual cycle of (*a*) sensible heat flux F_{sens} and (*b*) latent heat flux F_{lat}. The solid lines depict area-averaged values, and the dashed lines depict fluxes over the sea ice only. Also shown are the calculated fluxes of *Doronin* [1963] (solid circles), *Badgley* [1966] (pluses), *Leavitt et al.* [1978] (solid triangles), *Maykut* [1978] (solid squares), *Maykut* [1982] (solid diamonds), and *Makshtas* [1984] (crosses).

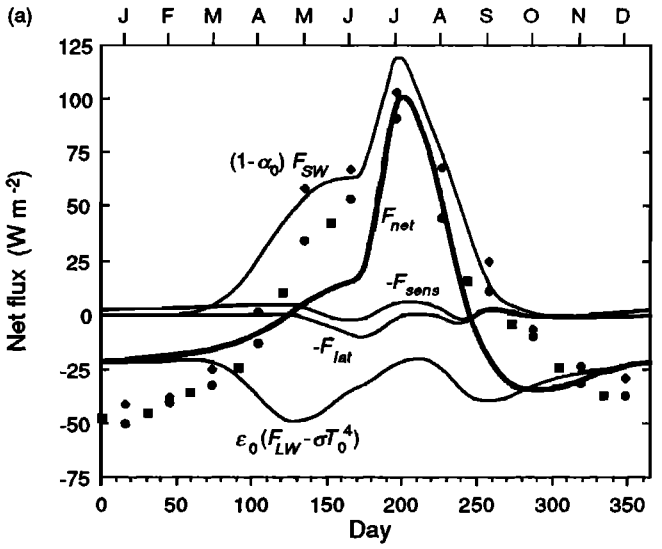

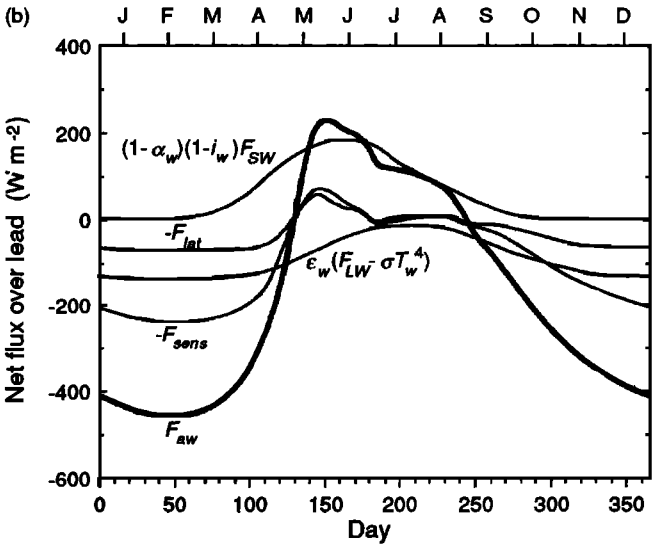

Fig. 9. Annual cycle of (*a*) area-averaged net flux at the surface and (*b*) net flux at the surface of a lead. Also shown are the calculations of *Maykut* [1978] (solid squares), *Maykut* [1982] (solid diamonds), and the model results of MU (solid circles).

Figure 9*b* shows the annual cycle of net flux at the surface of a lead and its components. Its evolution differs markedly from the area average in Figure 9*a*, which is dominated by the sea ice. During winter, F_{aw} is dominated by the loss of sensible heat, with the latent heat and net longwave fluxes playing lesser roles. In summer the sensible, latent, and net longwave fluxes are all near zero, and the energy input is governed almost entirely by the net shortwave flux, $(1-\alpha_w)(1-i_w)F_{SW}$.

3.7. *Lead Fraction*

The lead fraction, A, is shown in Figure 10, along with other values estimated from submarine sonar, reconnaissance flight, and satellite visible and summertime passive microwave observations. The model predicts a minimum value of $A = 0.009$ in late winter, and a maximum value of $A = 0.114$ in early September. There is enormous variation in the observations, with the two microwave estimates having the greatest late summer values of 0.22 [*Comiso*, 1990] and 0.26 [*Carsey*, 1982]. However, these two estimates may be affected by the signal from meltwater ponds [*Cavalieri et al.*, 1990]. Perhaps the most reliable estimate of lead fraction is that of *Asselin* [1977], which is based on over 20 years of British and Canadian sea ice maps compiled from aircraft and satellite data. When compared with these observations, averaged for 80°N, the model's predicted lead fraction is slightly low. This is a common failure of one-dimensional sea ice models [e.g., *Shine and Crane*, 1984; *Mellor and Kantha*, 1989], which by their nature cannot correctly incorporate the dynamic effects of ice divergence and ridging which are primarily responsible for the creation and enlargement of open water in the pack ice. Nevertheless, our modeled lead fraction appears to be reasonable.

3.8. *Basal Heat Flux*

The model's predicted heat flux at the base of the ice, F_b, is shown in Figure 11. It has values near zero during winter, increasing to 6.7 W m^{-2} in early August. This is almost entirely a

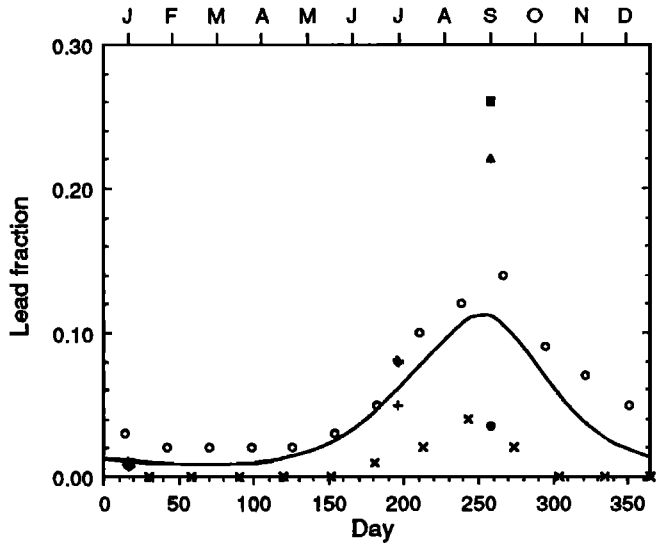

Fig. 10. Annual cycle of lead fraction A. Also shown are the passive microwave observations of *Carsey* [1982] (solid squares) and *Comiso* [1990] (solid triangles); aerial/satellite observations reported by *Asselin* [1977] (open circles), *Robock* [1980] (crosses), and *Weeks* [1976] (solid diamonds); and submarine sonar observations reported by *McLaren* [1986] (solid circles) and *Weeks* [1976] (pluses).

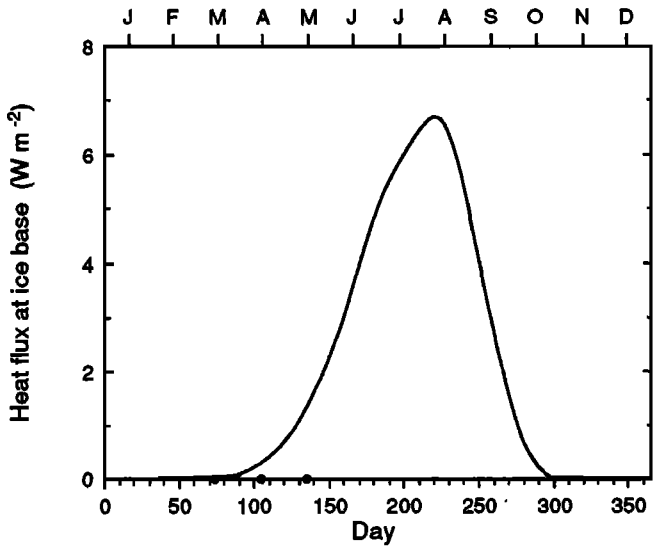

Fig. 11. Annual cycle of heat flux at the ice base F_b. Also shown are the observations of *McPhee and Untersteiner* [1982] (solid circles).

result of warming of the ocean mixed layer by solar radiation entering through the leads (Table 4). While it is acknowledged that the sea ice thickness is quite sensitive to the heat flux at the ice base [MU; *Shine and Henderson-Sellers*, 1985; *Harvey*, 1988*a*], there exist few measurements of F_b. Our predicted annual average of 1.8 W m^{-2} is in good agreement with the value of 2 W m^{-2} frequently used in models. *McPhee and Untersteiner* [1982] inferred near-zero values of F_b in the central Arctic in spring. Model results of *Häkkinen and Mellor* [1990] gave Arctic Ocean heat fluxes of F_b = 4-9 W m^{-2} in late summer, while *Fleming and Semtner* [1991] predicted a central Arctic heat flux of 5 W m^{-2} year-round. Recent measurements by *Perovich and Maykut* [1990] suggest that the summertime heat flux may be smaller than were previously expected [e.g., *Maykut and Perovich*, 1987] because the drainage of meltwater produces a cool, nearly fresh layer directly beneath the ice which inhibits the upward transport of heat into the ice.

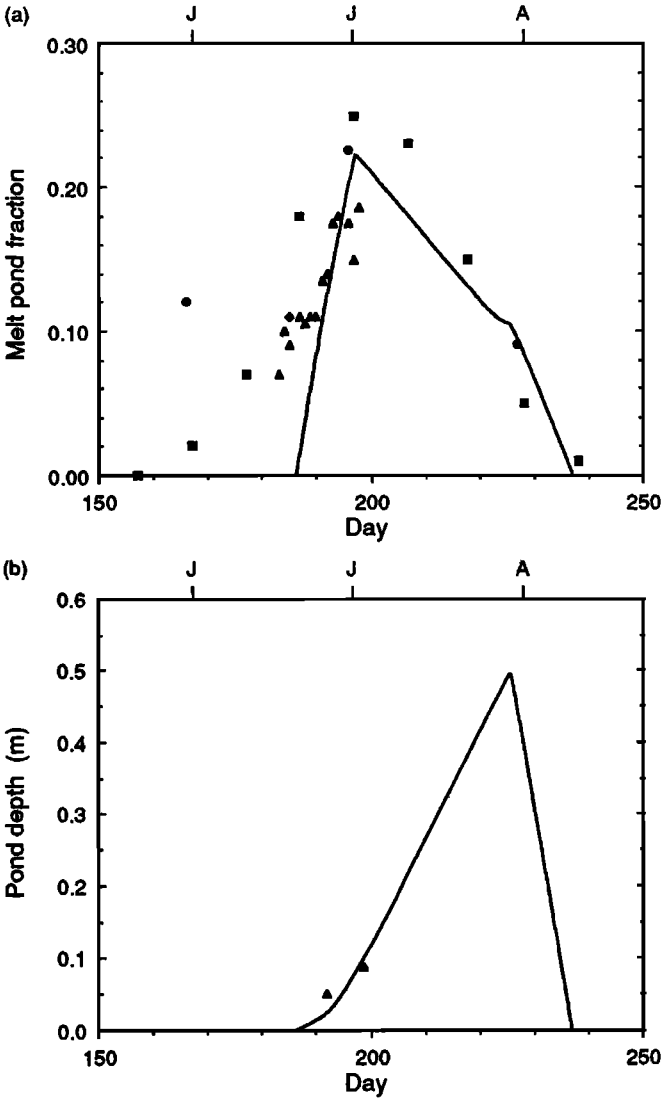

Fig. 12. Annual cycle of (*a*) meltwater pond fraction P and (*b*) pond depth h_p. Also shown are the pond fraction observations of *Nazintsev* [1964] (solid squares), *Chernigovskii* [1968] (solid circles), *Maykut and Perovich* [1985] (solid triangles) and *Francis et al.* [1991] (solid diamonds), and the pond depth observations of *Maykut and Perovich* [1985] (solid triangles).

3.9. *Meltwater Ponds*

Figure 12*a* shows the meltwater pond fraction P predicted by the model. Measurements of P reported by *Nazintsev* [1964] and *Chernigovskii* [1968] from Soviet drifting stations and by *Maykut and Perovich* [1985] and *Francis et al.* [1991] from multiyear sea ice observed during the Marginal Ice Zone Experiment (MIZEX) in 1984 are also shown. The model generally agrees well with the observations. Some difference occurs in the onset of pond formation, where the late onset of melting in the model leads to an underestimate of pond fraction in early summer.

The pond depth h_p is shown in Figure 12*b*. The model predicts an increase in h_p to its maximum depth of 0.53 m over a period of 1 month. The minimum integrated pond albedo is 0.14, which contributes to the decrease in average ice surface albedo from 0.61 to its minimum value of 0.47 (Figure 6). Measurements of melt pond depth are rare; two values of h_p observed in the Beaufort Sea by *Grenfell and Perovich* [1984] are plotted in Figure 12*b*. While these data are far from comprehensive, they suggest that the rate of increase in pond depth predicted by the model is reasonable. The

predicted pond depth of 0.53 m at the end of the melt season is probably too deep; however, the small horizontal extent minimizes the errors associated with this problem.

4. SENSITIVITY TO MODEL PARAMETERS AND EXTERNAL FORCING

In this section we investigate the extent to which uncertainties in the model parameters influence the outcome of the model integration, and therefore our confidence in the results. As in other sea ice model studies, we focus on the response of the equilibrium sea ice thickness $\langle h_i \rangle$ to changes in parameters. The fluxes at the surface and ice base are examined in an effort to explain the physical processes underlying the model's response. We also use the sea ice model to examine the sensitivity of the equilibrium sea ice thickness to changes in external (atmospheric and oceanic) forcing, with the purpose of further investigating the nature of the physical interactions and feedback processes contained within the sea ice-lead component of the polar climate system. In these experiments the sea ice model was not coupled with the cloud radiative model; i.e., the downward solar and longwave fluxes were prescribed (from Table 1) rather than computed interactively.

An ice thickness sensitivity parameter δ_{h_i} is defined as the scaled partial derivative,

$$\delta_{h_i}(\phi) = \frac{\overline{|\langle\phi\rangle|}}{\overline{\langle h_i \rangle}} \frac{\partial \langle h_i \rangle}{\partial \langle \phi \rangle} \tag{32}$$

where the overbar denotes the baseline value, angle brackets denote the annual average, and ϕ represents the parameter or external forcing variable in question. A positive value of $\delta_{h_i}(\phi)$ indicates that a positive change in ϕ will produce an increase in $\langle h_i \rangle$. Similarly, we define a flux sensitivity parameter δ_F as

$$\delta_F(\phi) = \frac{\overline{|\langle\phi\rangle|}}{\overline{|\langle F \rangle|}} \frac{\partial \langle F \rangle}{\partial \langle \phi \rangle} \tag{33}$$

where F is a flux which is directly or indirectly affected by the value of ϕ.

Let us consider how a change in any external parameter or forcing variable affects the internal variables and fluxes in the model. Figure 13 shows a network of interactions and feedback processes relating the model variables and fluxes (shown in ovals and boxes, respectively) to each other and to the prescribed values of the parameters and external forcing (shown in italic and bold type, respectively, around the perimeter of the diagram). The connecting arrows represent the model equations in section 2; a solid arrow indicates that a positive change in the first quantity has a direct positive impact on the value of the second (a positive interaction), while a short-dashed arrow signifies that a positive change in the first quantity produces a negative change in the second (a negative interaction). Long-dashed arrows represent interactions that can be either positive or negative, depending on season. Parameters and variables can interact indirectly via sequences of direct interactions involving intermediate variables.

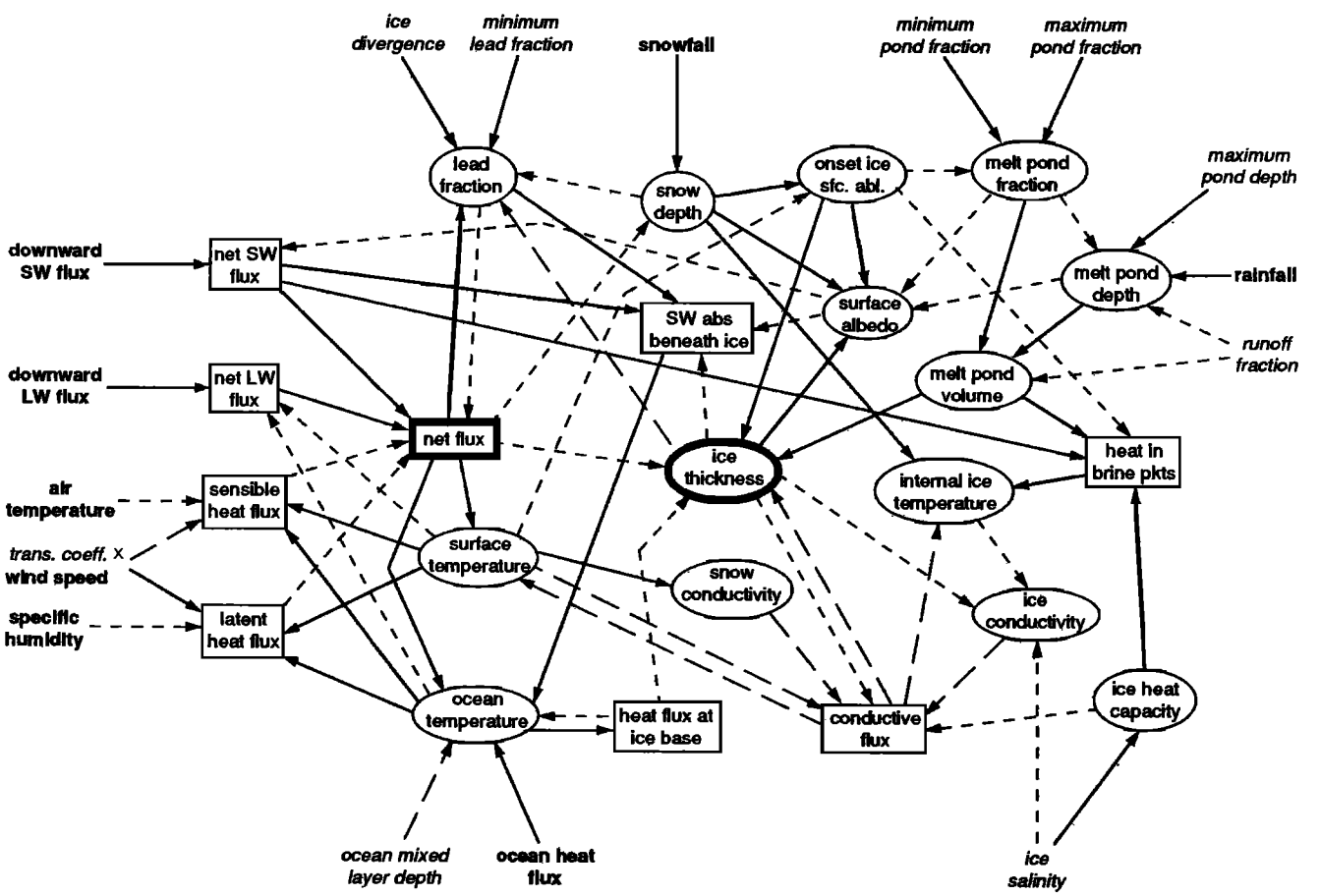

Fig. 13. Schematic of interactions between external forcing (bold) and parameter values (italics), and internal variables (ovals) and fluxes (boxes). The solid arrows represent positive interactions (an increase in the first quantity leads to an increase in the second quantity), the short-dashed arrows- represent negative interactions (an increase in the first quantity leads to a decrease in the second quantity), and the long-dashed arrows represent interactions that may be positive or negative, depending upon the season. The net flux and ice thickness are highlighted to emphasize their importance.

Furthermore, the interactions can be amplified or dampened via positive and negative feedback loops. A positive, or amplifying, feedback loop consists of a cycle of consecutive variables and fluxes containing an even number of negative interactions, so that a change in the value of a variable leads to a further change in that variable in the same sense. A negative feedback loop contains an odd number of negative interactions, so that a given change in a variable produces a reduction in the original change to that variable. A negative feedback loop thus dampens the response of the system. A system governed by positive feedback loops is unstable and does not converge to an equilibrium state, but instead grows without bound or produces oscillatory behavior. Negative feedbacks dampen the growth or oscillations so that an equilibrium state may eventually be attained. The stronger the negative feedbacks, the sooner equilibrium is reached.

The computed values of the sensitivity parameters, $\delta_{h_i}(\phi)$ and $\delta_F(\phi)$, are the net result of all relevant direct and indirect interactions, modulated by various positive and negative feedbacks. Because of the complexity and nonlinearity of the model, we have not attempted a quantitative linear feedback analysis of the variety frequently used to investigate feedbacks in climate models [e.g., *Schlesinger*, 1985; *Harvey*, 1988*b*]. Such a feedback analysis assumes that the feedback processes are independent and additive; Figure 13 shows that the first assumption is invalid for this sea ice model. Rather, we will discuss the results of the sensitivity tests in light of the most important interactions and feedbacks, and generally in a qualitative sense. The feedback processes were identified from Figure 13 and by examining the signs and magnitudes of the flux sensitivity parameters.

4.1. *Sensitivity to Parameters*

Of the 16 model parameters listed in the notation section, several have values which are not well known. Multiple model runs were made varying one parameter at a time within a plausible range of values while holding the others constant at their baseline values. This procedure, although time-consuming, yields the sensitivity of the model results to each parameter, independent of the others. In reality, some parameters may be correlated (for example, an increased maximum pond fraction might be related to a decrease in runoff); we have not attempted to investigate these effects.

Table 5 lists nine parameters which we considered to have sufficiently uncertain values to warrant further investigation, along with the sensitivity parameters, δ_{h_i} and δ_F. The dependence of $\langle h_i \rangle$ on the parameters values is shown in Figure 14 for plausible ranges of parameter values. In some cases the results of extreme variations in a parameter will be described. The slope of each curve reflects the sensitivity of $\langle h_i \rangle$ to the value of that parameter, ϕ. A large sensitivity can occur if the relevant processes directly affecting the ice thickness are strongly sensitive to ϕ, or if strong positive feedback loops (or only weak negative feedback loops) are operating. Changes in slope occur when different physical processes dominate for different ranges of ϕ. An example of this behavior is seen in Figure 14*h*.

Table 5 shows that the equilibrium sea ice thickness is most sensitive to variations in runoff fraction f_{RO} and sea ice divergence D, while no sensitivity is shown for the ocean mixed layer depth d_w. The remaining parameters are associated with moderate sensitivities, δ_{h_i}.

Figure 14*a* through 14*d* show the dependence of $\langle h_i \rangle$ on four parameters contained in the melt pond parameterization. The sea ice thickness depends moderately on the values of P_{max} and P_{min}. Larger values of these two parameters lead to smaller ice thickness by reducing the surface albedo, and therefore increasing the net shortwave flux into the surface ($\delta_{F_{SWnet}} > 0$), during the melt season. This process is called the surface albedo feedback. Even though a greater volume of meltwater can potentially be retained for refreezing, this is more than compensated by the additional surface melting. For a maximum pond fraction greater than about 0.55, the ice melts completely away during summer (Figure 14*b*). An increase in h_{pmax} also lowers the surface albedo, but in this case the increased retention of surface water is the dominant effect. Since the pond depth never exceeds 0.53 m, increases in h_{pmax} beyond 0.53 m have no effect on the model results.

Figure 14*d* shows that f_{RO} has a large influence on the ice thickness. In fact, the large uncertainty regarding the appropriate value of f_{RO}, combined with the sensitivity of $\langle h_i \rangle$ to the prescribed value of f_{RO}, permitted us to use this parameter to tune the model. Realistic values of $\langle h_i \rangle$ were produced for f_{RO} in the range 0.6-0.9. The runoff fraction has its greatest impact in the early part of the melt season, when increasing f_{RO} allows less water to remain in melt ponds on the surface, increasing the average albedo and reducing the net shortwave flux. If melt ponds are completely omitted ($P_{max} = 0$, $h_{pmax} = 0$, or $f_{RO} = 1$), the surface albedo increases to the bare ice value, reducing the net shortwave flux over the ice by 15 W m^{-2} and leading to an equilibrium ice thickness of 5.0 m. For values of runoff fraction less than 0.5, the increased net flux corresponding to a darker surface is large enough to melt the ice completely for a few weeks in summer, producing a mean annual thickness of approximately 0.8 m. The surface albedo feedback is thus the primary mechanism by which the values of the melt pond parameters influence the sea ice thickness.

Two parameters involved in the lead parameterization are varied in Figures 14*e* and 14*f*. As the ice divergence D is increased (Figure 14*e*), $\langle h_i \rangle$ decreases from a value of 4.3 m for $D = 2.0 \times 10^{-9}$ s^{-1} to a value of 2.1 m for $D = 6.5 \times 10^{-9}$ s^{-1}. An increased ice divergence (transport) increases the year-round rate of lead opening

TABLE 5. Sensitivity of Equilibrium Sea Ice Thickness, $\langle h_i \rangle$, and Relevant Annual Average Fluxes, $\langle F \rangle$, to Model Parameters

Parameter	Range of Values (Baseline)	δ_{h_i}	δ_F
Minimum meltwater pond fraction P_{min}	0.00 - 0.25 (0.10)	-0.17	$\delta_{F_{SWnet}} = 0.01$
Maximum meltwater pond fraction P_{max}	0.15 - 0.80 (0.25)	-0.27	$\delta_{F_{SWnet}} = 0.01$
Maximum meltwater pond depth h_{pmax}	0.1 - 1.0 m (0.8 m)	0.00	$\delta_{F_{SWnet}} = 0.00$
Meltwater runoff fraction f_{RO}	0.40 - 0.90 (0.85)	1.30	$\delta_{F_{SWnet}} = -0.06$
Sea ice divergence D	2.0×10^{-9} - 6.5×10^{-9} s^{-1} (4.5×10^{-9} s^{-1})	-0.70	$\delta_{F_{wi}} = 1.15$; $\delta_{F_b} = 1.25$
Minimum lead fraction A_{min}	0.000 - 0.030 (0.005)	0.00	$\delta_{F_{wi}} = 0.00$; $\delta_{F_b} = 0.00$
Ocean mixed layer depth d_w	10 - 100 m (30 m)	0.00	$\delta_{F_b} = 0.00$
Bulk heat and moisture transfer coefficient over ice for neutral stability, C_{TO}	0.5×10^{-3} - 3.0×10^{-3} (1.3×10^{-3})	0.21	$\delta_{F_{sens}} = -1.97$; $\delta_{F_{lat}} = 0.35$
Salinity of multiyear sea ice, S_i	1.0 - 4.5 ppt (3.2 ppt)	-0.06	$\delta_{F_c} = 0.03$

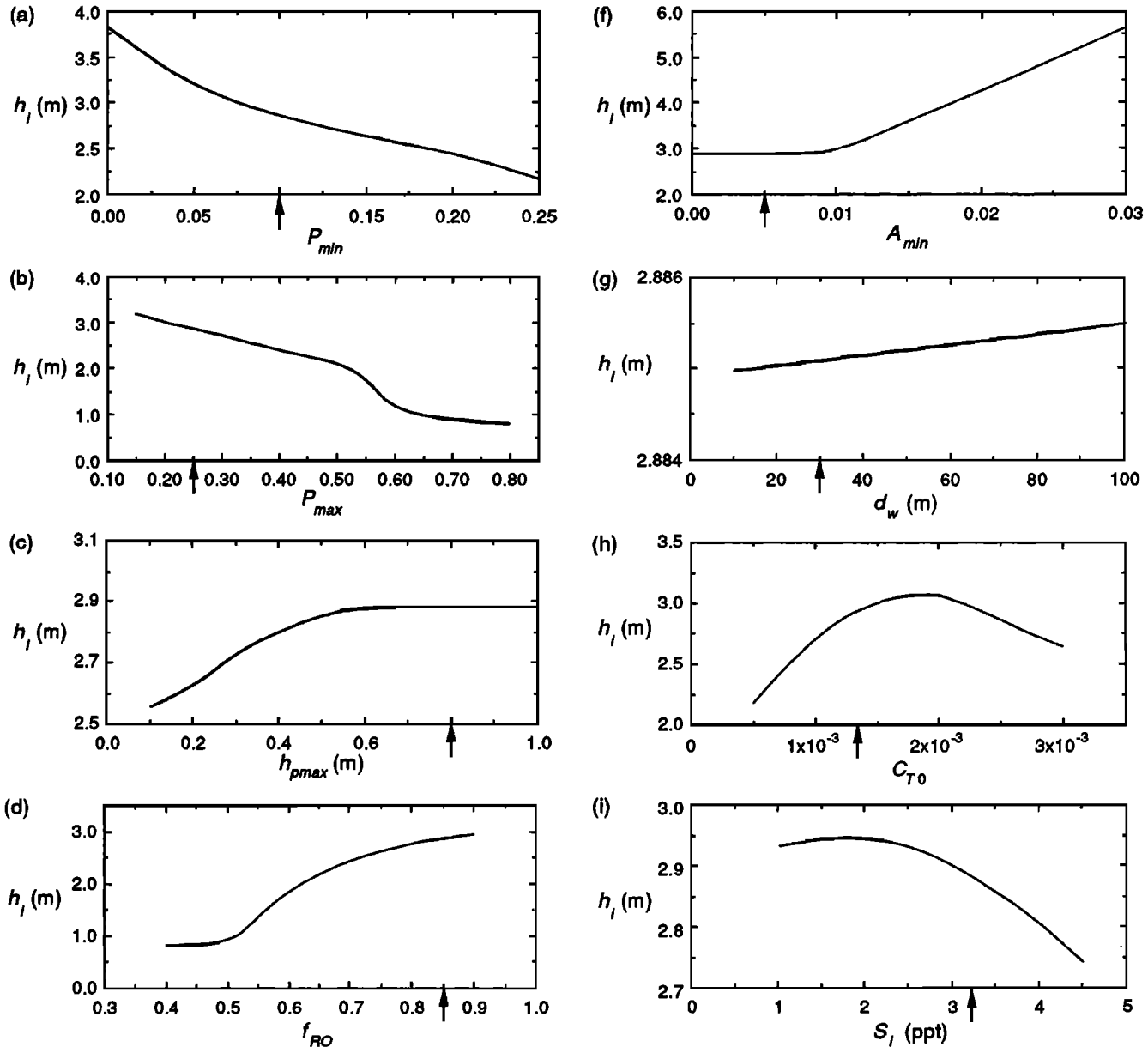

Fig. 14. Dependence of equilibrium ice thickness on model parameters: (*a*) minimum melt pond fraction P_{min}, (*b*) maximum melt pond fraction P_{max}, (*c*) maximum melt pond depth h_{pmax}, (*d*) runoff fraction f_{RO}, (*e*) ice divergence D, (*f*) minimum lead fraction A_{min}, (*g*) ocean mixed layer depth d_w, (*h*) bulk transfer coefficient C_{T0}, and (*i*) multiyear ice salinity S_i. The arrows indicate the baseline values of the parameters.

via (8), with two opposing effects. A larger fraction of open water allows greater cooling of the ocean mixed layer in winter, resulting in enhanced lateral and basal accretion (and ridging if A falls below A_{min}), while in summer enhanced absorption of solar radiation ($\delta_{F_{wi}} > 0$) increases the rate of both lateral and basal melting. This negative summertime interaction dominates over the positive wintertime process, especially for large values of D. In sensitivity tests of a one-dimensional sea ice model coupled to a detailed ocean mixed layer model, *Mellor and Kantha* [1989] also found a strong negative dependence of equilibrium sea ice thickness on prescribed divergence rate. If sea ice transport is neglected ($D = 0$), an unreaslistically large ice thickness of 11 m results.

Figure 14*f* shows the modeled equilibrium sea ice thickness increasing sharply with prescribed minimum lead fraction for values of A_{min} greater than about 0.009 (for $A_{min} = 0$, the value of A did not fall below 0.009). A similar model sensitivity was found by *Ledley* [1987, 1988], who investigated the sensitivity of a one-dimensional thermodynamic sea ice model to the prescribed minimum lead fraction. The minimum lead fraction constraint, or ridging process, is normally invoked only during winter when

successive months of surface cooling have produced enough lateral ice accretion to nearly close the leads. Thus the wintertime basal ice accretion mechanism is directly affected by the value of A_{min}, as greater cooling of the ocean mixed layer in wider leads causes $\delta_{F_b} < 0$. However, an indirect response occurs in summer as the thicker ice produced by enhanced wintertime accretion favors lateral, rather than basal, accretion (equation (23)); the date of maximum lead fraction is later in the summer, and a smaller solar flux penetrates to the level below the ice ($\delta_{F_{wi}} < 0$). It is the resulting reduction in bottom ablation that is responsible for increasing the value of $\langle h_i \rangle$. (In fact, the annual bottom accretion actually decreases for increasing A_{min}, although an increasingly greater proportion of the accretion occurs via ridging.)

The mixed layer depth d_w is varied in Figure 14*g*, with very little change in $\langle h_i \rangle$. A deeper mixed layer has a greater thermal inertia so that the water stays warmer longer in the fall and cooler longer in the spring. This results in nearly compensating enhancements in ice ablation and accretion, with the accretion having a slight advantage, presumably due to length of season. A more realistic ocean mixed layer model with variable temperature and salinity profiles would have stronger interactions with the sea ice.

The heat transfer coefficient over bare ice, C_{T0}, directly influences the magnitude of the turbulent sensible and latent heat fluxes (equation (29)). Values of C_{T0} encountered in the literature range from 0.55×10^{-3} to 3.0×10^{-3} for bare sea ice. Figure 14*h* shows the effect on $\langle h_i \rangle$ of varying C_{T0} across this range. As C_{T0} is increased, the magnitudes of the sensible and latent heat fluxes are also increased, most significantly the downward sensible heat flux ($\delta_F < 0$), resulting in an increased net flux at the surface. For larger C_{T0} the enhanced F_{sens} produces a thinner ice cover. However, a strong negative feedback curtails the sensitivity of $\langle h_i \rangle$ to C_{T0}, namely, the increased downward sensible heat flux warms the surface, which then weakens the temperature gradient and reduces the magnitude of the flux. A similar feedback involving the latent heat flux also occurs but is much less effective because the wintertime values of F_{lat} are small. Together these are called the turbulent flux feedback. For smaller values of C_{T0}, the turbulent flux feedback is less effective and thermodynamic processes dominate the sea ice behavior. When C_{T0} is decreased, a cooler surface in winter and spring leads to increased heat conduction from the warmer ocean; late in the spring the enhanced conduction causes the surface to warm faster, accelerating the onset of the melt season and producing a thinner ice slab. This initiates a conduction feedback, where a thinner ice cover experiences greater conduction of heat from the ocean through the ice throughout most of the year, contributing to further surface warming and earlier onset of melting.

The sea ice thickness is only weakly sensitive to the prescribed multiyear ice salinity S_i, as can be seen in Table 5 and Figure 14*i*. The salinity affects the ice conductivity and heat capacity (equations (11) and (12)), but significantly only when the temperature is near freezing, that is, near the ice base and during summer when brine pockets are present. For larger values of S_i, the smaller ice conductivity and greater heat capacity lead to reduced ablation and accretion rates at both surfaces, with the decrease in bottom accretion being slightly dominant.

Sensitivity experiments were run for the atmospheric and ocean turbulence parameters, b' and b, but produced negligible variations in $\langle h_i \rangle$. The remaining parameters in the notation section were not considered be sufficiently uncertain to necessitate sensitivity tests.

We believe we have chosen the most reasonable set of parameter values for use in this one-dimensional sea ice model, based on the physical measurements and theoretical calculations reported in the meteorological and oceanographic literature. However, we did not vary more than one parameter at a time in our sensitivity tests, and it may be that there are other, possibly better, sets of parameter values which will produce realistic sea ice behavior. Nevertheless, in Table 6 we give the parameter ranges which produce realistic values of equilibrium sea ice thickness ($\langle h_i \rangle$ between 2 and 4 m) in our sensitivity tests.

TABLE 6. Parameter Values Which Produce Equilibrium Sea Ice Thickness, $\langle h_i \rangle$, Between 2 and 4 m

Parameter	Range of Values
P_{min}	0.00 - 0.25
P_{max}	0.15 - 0.52
h_{pmax}	0.1 - 1.0 m
f_{RO}	0.62 - 0.90
D	2.5×10^{-9} - 6.5×10^{-9} s^{-1}
A_{min}	0.000 - 0.018
d_w	10 - 100 m
C_{T0} (ice)	0.5×10^{-3} - 3.0×10^{-3}
S_i	1.0 - 4.5 ppt

4.2. *Sensitivity to External Forcing*

Here the sea ice model is used to examine the sensitivity of $\langle h_i \rangle$ to changes in external forcing in order to further investigate the nature of the interactions and feedback processes. Because the atmosphere and ocean in our model cannot respond to changes in sea ice conditions, we generally limit these sensitivity tests to small variations in external forcing. Again, we vary only one forcing variable at a time, although we acknowledge that any realistic climate change would involve simultaneous changes in all of the forcing variables. We emphasize that the results of these sensitivity experiments cannot be interpreted as an estimate of the response of sea ice thickness to changes in global climate because no three-dimensional atmospheric or oceanic feedbacks are considered.

Values of δ_{h_i} and δ_F are listed in Table 7 for eight external forcing variables. To show the dependence of ice thickness on the individual forcing variables, plots of $\langle h_i \rangle$ versus ϕ are presented in Figure 15.

The model's equilibrium sea ice thickness is extremely sensitive to changes in the downward longwave flux F_{LW} and the air temperature T_a, undergoing complete melting in summer for an increase in F_{LW} greater than 2% or an increase in T_a greater than 1°C. A similar response to increasing prescribed air temperature was also found by *Semtner* [1987]. The ice thickness is also highly sensitive to the shortwave flux F_{SW} and atmospheric humidity q_a. It is moderately sensitive to the ocean heat flux F_{ocean} and insensitive to small variations in wind speed, u_a, snowfall, SF, and rainfall, RF.

Looking first at the downward radiative fluxes, Figures 15*a* and 15*b* show the response of $\langle h_i \rangle$ when F_{SW} and F_{LW} are varied between 95% and 105% of their baseline values. A change in downward longwave flux has a much greater effect on $\langle h_i \rangle$ than an equivalent fractional change in downward shortwave flux because F_{LW} acts throughout the year, whereas F_{SW} is important mainly during spring and summer, and a large percentage of the incoming solar flux is lost to surface reflection.

Several negative interaction sequences and positive feedback loops contribute to the large sensitivity of $\langle h_i \rangle$ to changes in radiative forcing. Increasing F_{SW} or F_{LW} acts primarily to increase the net flux over the ice, which warms the ice surface. A warmer surface accelerates the onset of surface melting, which lowers the

TABLE 7. Sensitivity of Equilibrium Sea Ice Thickness, $\langle h_i \rangle$, and Annual Average Fluxes, $\langle F \rangle$, to Model Forcing

Parameter	Range of Variation About Baseline	δ_{h_i}	$\delta_{F_{net}}$	$\delta_{F_{SWnet}}$	$\delta_{F_{LWnet}}$	$\delta_{F_{sens}}$	$\delta_{F_{lat}}$	$\delta_{F_{wi}}$	δ_{F_b}	δ_{F_c}
F_{SW}	± 5%	-9.64	4.38	1.44	-1.85	-19.72	-6.30	6.34	7.45	9.56
F_{LW}	± 5%	-41.55	-41.39	2.47	-8.18	-44.17	-10.85	12.82	13.59	20.41
T_a	±2°C	-23.99*	60.80*	2.32*	-2.69*	-48.79*	-12.58*	7.93*	8.35*	13.24*
q_a	± 5%	-6.59	18.33	0.83	-1.08	-9.08	-14.67	2.81	3.07	5.00
u_a	± 50%	-0.19	-1.06	-0.16	-0.43	-7.93	-0.57	-0.33	-0.36	-0.46
RF	± 100%	-0.00	0.00	0.00	0.00	-0.00	-0.00	0.00	0.00	0.00
SF	± 100%	-0.14	1.14	-0.04	0.09	-0.09	-0.01	0.05	0.05	-0.19
F_{ocean}	0 - 5 W m^{-2}	-1.04†	0.03†	0.01†	-0.05†	-0.49†	-0.18†	0.23†	0.83†	0.25†

*In computing the sensitivities to T_a, the baseline annual air temperature range of 26.5°C was used in scaling instead of the annual average air temperature of 259.8 K.

†In computing the sensitivities to F_{ocean}, a value of 1 W m^{-2} was used for scaling, rather than the baseline value of 0 W m^{-2}.

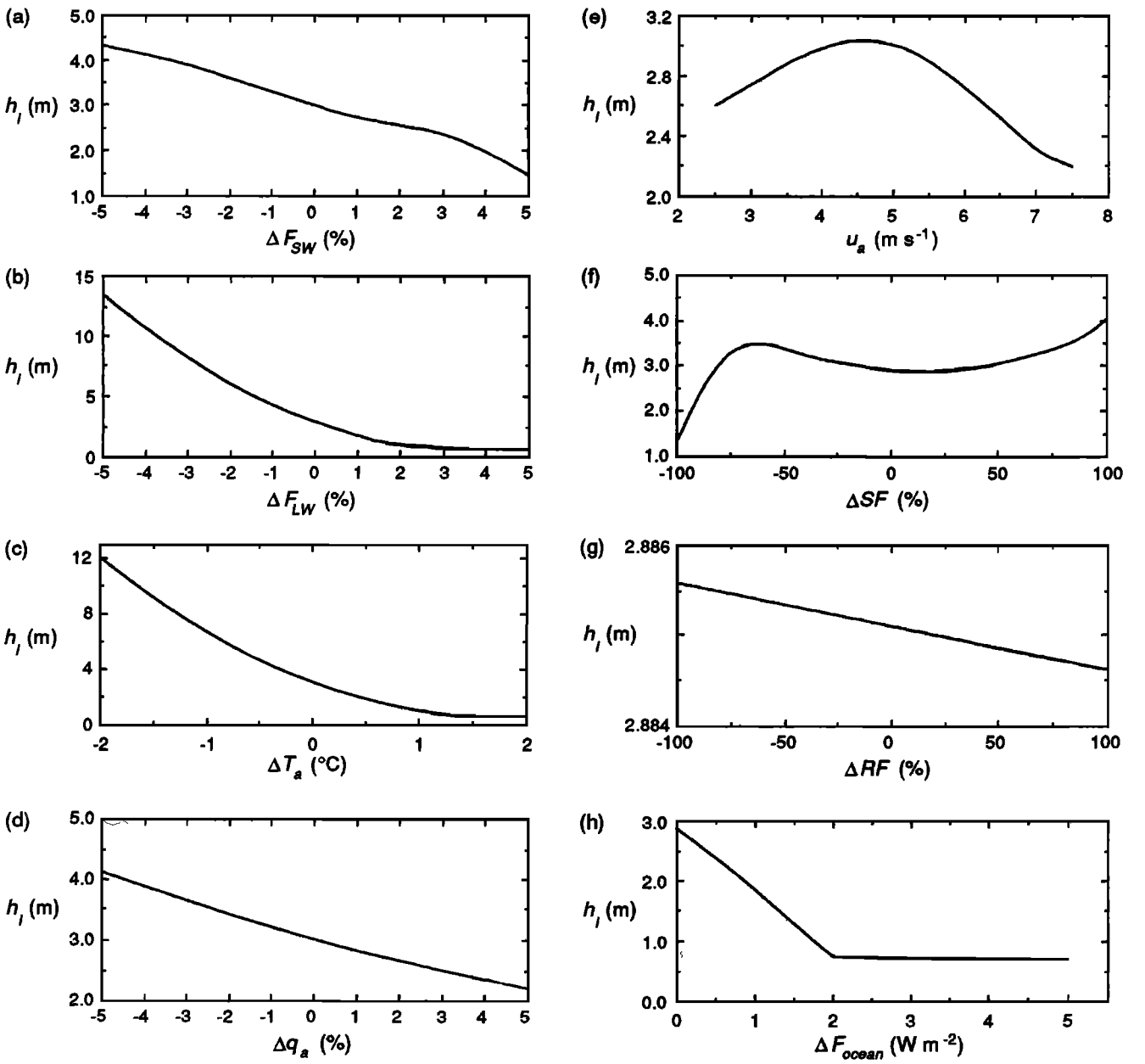

Fig. 15. Dependence of equilibrium ice thickness on external forcing: (*a*) downward shortwave flux F_{SW}, (*b*) downward longwave flux F_{LW}, (*c*) air temperature T_a, (*d*) specific humidity q_a, (*e*) wind speed u_a, (*f*) snowfall SF, (*g*) rainfall RF, and (*h*) ocean heat flux F_{ocean}.

surface albedo and increases the net shortwave flux. This represents the surface albedo feedback and is illustrated in Figure 16*a*. The ice ablation is increased directly as a result of the greater energy input, and indirectly through a lowering of the surface albedo with decreasing ice thickness, increasing melt pond extent and depth, and delay of snow accumulation. The conduction feedback is also activated, as the conduction of heat from the ocean through the ice is greater for a thinner ice cover ($\delta_{F_c} > 0$), contributing further to surface warming and melting. This feedback loop is shown in Figure 16*b*.

An increase in F_{SW} directly increases the solar flux absorbed by the water below the ice ($\delta_{F_{wi}} > 0$), which enhances the basal ablation rate via F_b. F_{wi} is also increased indirectly when F_{SW} or F_{LW} are increased because the thinner ice allows a greater proportion of the solar flux entering the ocean to be absorbed below the level of the ice. This mechanism, which we call the lead solar flux feedback (Figure 16*c*), explains why $\delta_{F_{wi}}(F_{LW}) > \delta_{F_{wi}}(F_{SW})$ even though the atmospheric shortwave flux was not changed in the former experiment. A thinner ice cover experiences greater lateral ice ablation and accretion, leading to a greater lead fraction in summer and a smaller lead fraction in winter. This allows more solar radiation to be absorbed by the ocean in summer and insulates the ocean more effectively in winter (resulting in $\delta_{F_{sens}} < 0$ and $\delta_{F_{lat}} < 0$, in spite of the ice surface being warmer), both of which contribute to a warmer ocean mixed layer and greater F_b. This process is designated the lead fraction feedback and is illustrated in Figure 16*d*.

Two strong negative feedbacks involving the surface temperature curtail the effects of the positive feedbacks described above. The increase in the outgoing longwave flux from the warmer surface ($\delta_{F_{LWnet}} < 0$) outweighs the influences of the shortwave and turbulent fluxes and produces an overall negative change in the surface net flux, thus acting as a cooling influence. This feedback will be called the outgoing longwave flux feedback. The other relevant negative feedback is the turbulent flux feedback introduced previously, which is operative over the sea ice. The warmer surface increases the sensible and latent heat fluxes, which decrease the surface net flux and leads to surface cooling. These two feedback loops are shown schematically in Figures 16*e* and 16*f*.

Many of the same negative interactions and positive feedback processes contribute to the decrease in $\langle h_i \rangle$ with increasing atmospheric temperature T_a or humidity q_a (Figures 15*c* and 15*d*). Except for $\delta_{F_{net}}$, all of the flux sensitivity parameters for T_a and q_a have the same sign as they had for F_{SW} and F_{LW}. However, the relative importance of the feedbacks differs for each of the forcing variables.

When T_a is increased, the increase in the downward sensible heat flux far outweighs any other effect, so that the surface net flux is also increased in spite of the increased longwave emission from the warmer surface. The negative feedback between the surface temperature and the sensible heat flux is weakened by the increased atmospheric stability. Similar arguments hold for the case of increasing atmospheric humidity q_a, except that in this case the latent heat flux is greatly decreased relatively more than the sensible heat

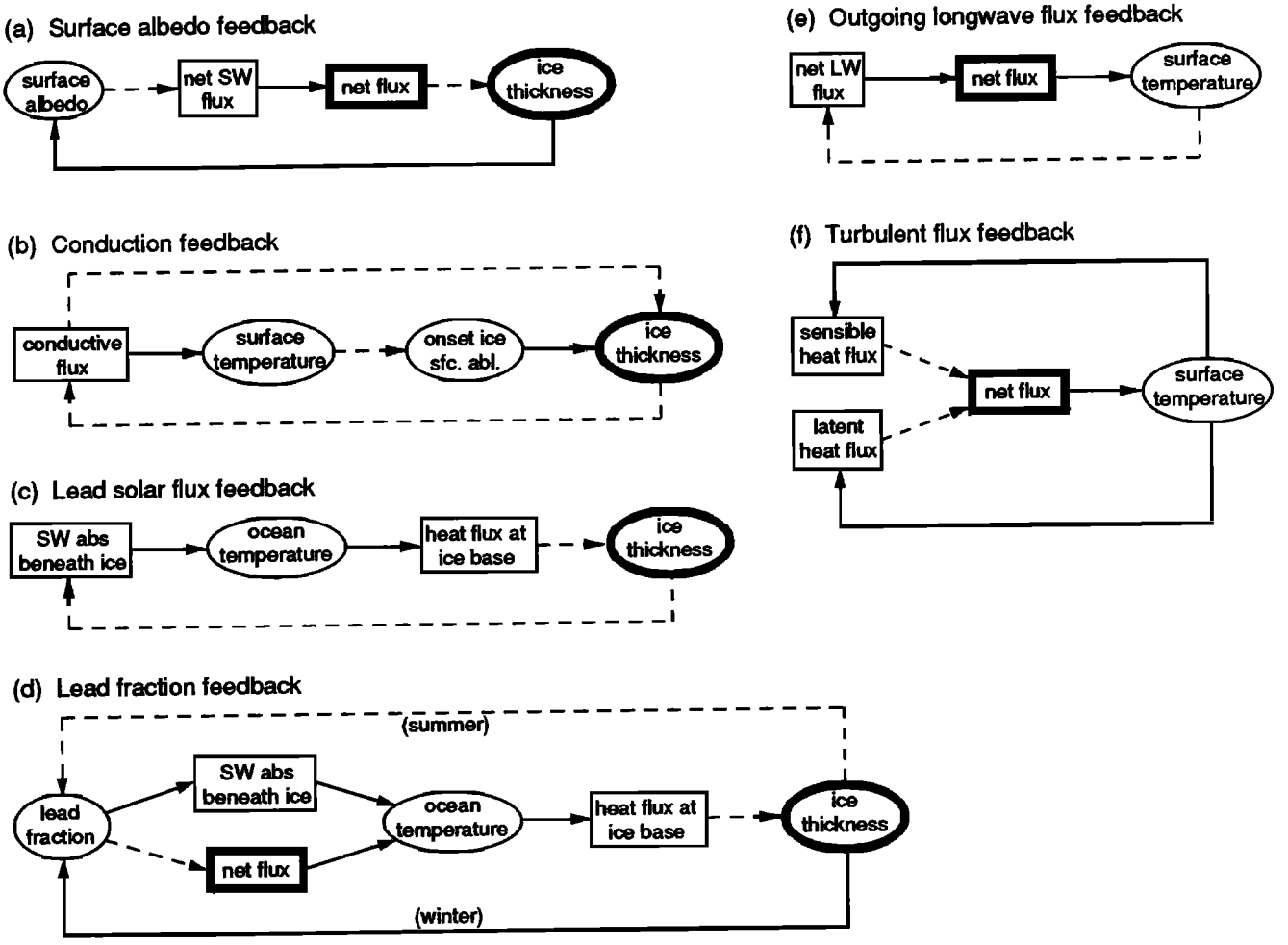

Fig. 16. Feedback processes occurring in the sea ice-lead system: (*a*) Surface albedo feedback, (*b*) conduction feedback, (*c*) lead solar flux feedback, (*d*) lead fraction feedback, (*e*) outgoing longwave flux feedback, and (*f*) turbulent flux feedback.

flux. Thus the turbulent flux feedback is disabled, while the positive feedbacks involving the surface albedo, conduction, lead solar flux and lead fraction all contribute to a further decrease in sea ice thickness. (However, we must point out that an arbitrary increase of 2°C in air temperature produces unrealistically large changes in the sensible heat flux; in reality the surface and air temperatures track each other closely. A one-dimensional model with a noninteractive atmosphere overemphasizes the strength of the negative turbulent flux feedback.)

Varying the prescribed wind speed u_a acts in much the same way as varying C_{T0}. The curves in Figures 14*h* and 15*e* are similar; both initially show a rapid increase in $\langle h_i \rangle$ toward a peak in the vicinity of the baseline value of u_a or C_{T0}, followed by a more gradual decline in the value of $\langle h_i \rangle$. An increase in wind speed increases both the downward sensible heat flux over the sea ice and the upward sensible heat flux over the leads, with compensating warming and cooling effects. Also, the stronger the surface wind, the more efficient the negative turbulent flux feedback is at dampening the positive feedbacks. The result is a small sensitivity of sea ice thickness to variations in wind speed near or greater than the baseline value. For u_a decreasing toward zero, the stabilizing turbulent flux feedback is less effective and enhanced winter and springtime heat conduction lead to earlier surface melting and greater ice ablation. In addition, the reduced turbulent heat loss from the leads prevents the leads from refreezing as quickly, resulting in a greater fraction of open water throughout the year. This allows the lead solar flux feedback to act, with more solar radiation penetrating into the ocean and contributing toward warming and melting.

Figure 15*f* shows the dependence of equilibrium sea ice thickness on prescribed snowfall. As was discussed by *Ledley* [1991], snow cover has two opposing influences on the sea ice. First, because of its poor conduction as compared with ice, snow acts as an insulator. An increase in snow depth results in reduced conduction and heat loss from the sea ice during the cold season. The warmer ice experiences less accretion and greater ablation at its bottom surface (the conduction feedback) as well as enhanced ablation at its upper surface in midsummer. A positive interaction operates in spring and summer, where a deeper snow layer requires more time to melt. This not only delays the onset of ice surface melting, it also increases the surface albedo, thereby reducing the net shortwave flux and the net energy input to the surface, causing the ice to grow thicker (the surface albedo feedback). The negative values of $\delta_{F_c}(SF)$ and $\delta_{F_{SWnet}}(SF)$ in Table 7 indicate that both the conduction and albedo feedbacks are operative for values of SF near the baseline; Figure 15*f* shows that they compensate almost exactly when the baseline snowfall is prescribed. For very small or very large snowfall the surface albedo feedback is dominant, as was also found by *Ledley* [1991].

The prescribed rainfall has only a very minor influence on the equilibrium sea ice thickness (Figure 15*g*). An increase in RF increases the rate of melt pond deepening. This reduces the surface albedo, increases the net flux, and enhances the surface ablation via the surface albedo feedback. The influence of RF is negligible, however, since the amount of rainfall is small, the majority of the rain is lost as runoff, and the melt ponds are in a growing phase for a period of only 1 month.

The dependence of $\langle h_i \rangle$ on ocean heat flux, F_{ocean}, is shown in Figure 15*h*. The larger the ocean heat flux, the warmer the ocean mixed layer. While some of this heat escapes through the leads, much of it goes to increasing the flux at the ice base ($\delta_{F_b} > 0$) and melting a greater amount of basal ice during summer and fall. The thinner ice then takes part in the feedback loops discussed earlier. When F_{ocean} is 3 W m^{-2} or greater, the sea ice cover melts completely during summer, producing a mean annual ice thickness of about 0.75 m. MU, *Semtner* [1984], *Ledley* [1985], and *Harvey* [1988*a*] have all used thermodynamic sea ice models to investigate the sensitivity of ice thickness to the value of the basal heat flux, F_b. To compare our results with theirs, we divide $\delta_{h_i}(F_{ocean})$ by $\delta_{F_b}(F_{ocean})$ to estimate a value of -0.43 for $\delta_{h_i}(F_b)$. (This is not strictly correct since other processes also contribute to F_b, but it gives a rough estimate of $\delta_{h_i}(F_b)$.) This sensitivity is smaller in magnitude than the corresponding sensitivities of -0.53, -0.62 and -0.79 estimated from the results of MU, Semtner, and Ledley, respectively, but greater than Harvey's sensitivity of -0.19. Notably, Harvey's model is the only one of the four to include leads. This illustrates the importance of the open water in modulating the Arctic ocean-air heat exchange.

5. CONCLUSIONS

An intermediate one-dimensional thermodynamic sea ice model has been presented that reproduces the annual cycle of sea ice growth and decay and addresses many of the uncertainties inherent in the thermodynamic sea ice model of *Maykut and Untersteiner* [1971]. In particular, we have introduced an albedo parameterization that is highly sensitive to the surface state. An essential component is a new melt pond parameterization which allows for a fractional area of meltwater ponds of variable depth during midsummer. A lead parameterization and prescribed sea ice divergence rate partially account for the effects of ice dynamics in a one-dimensional model. The inclusion of leads also allows for the absorption of solar radiation in the ocean, resulting in a more realistic time-varying basal heat flux at the lower surface of the ice.

The model generally performed quite well in predicting the current climatic sea ice conditions in the central Arctic when compared with observations and other theoretical calculations. The annual cycles of ice thickness and temperature are well within the range of observed values, and the aerially averaged albedo matches well with the most recent satellite observations from the central Polar Basin. The net longwave and shortwave fluxes at the surface are in reasonable agreement with other calculations. The calculated sensible and latent heat fluxes were smaller in magnitude than other calculations reported in the literature; however, we believe this is not an error but rather a result of (1) the use of a more appropriate heat transfer coefficient during the very stable wintertime conditions and (2) the inclusion of fluxes over leads in the aerial average. The annual cycles of lead fraction, basal heat flux, and melt pond area and depth all appear to be reasonable when compared with the small number of available observations.

A number of sensitivity tests were conducted to determine the extent to which tuning of model parameters contributed to the model's success in reproducing the observed sea ice annual cycle. The model was quite sensitive to the values of ice divergence D and minimum lead fraction A_{min}, producing large ice thicknesses for small values of D or large values of A_{min} as a result of positive feedback mechanisms involving cooling of water in the leads. The ice thickness was also quite sensitive to the prescribed runoff fraction f_{RO} and moderately sensitive to the other parameters in the melt pond parameterization. This sensitivity results from the strong dependence of surface albedo, and hence net flux, on the surface conditions. No more than one parameter was varied at a time, so therefore we cannot be certain to have found the optimal set of parameter values for matching model results with observations. However, for each parameter we chose the value we felt was most appropriate, based on observational data reported in the literature. As very little has been written concerning surface runoff, the runoff fraction f_{RO} was used to tune the model. *Maykut and Untersteiner*

[1971, p.1556] state that "at least one half of the melt ponds drain," providing some support for our final choice of f_{RO}=0.85. More observations of the surface runoff, melt pond extent and depth, and especially pond spectral albedo are needed before the accuracy of the melt pond parameterization can be validated and improved.

To investigate the nature and importance of the physical interactions and feedback processes governing the sea ice-lead system, individual sensitivity tests were run for each of the external forcing variables. These experiments should not be construed as predictions of the sea ice response to climatic change because (1) a realistic climate change scenario would involve simultaneous changes in all of the forcing variables, and (2) the use of a prescribed atmospheric state, rather than interactive one, precludes the expression of a number of important feedback processes. Nevertheless, these experiments highlight several relevant physical interactions and feedbacks which must be properly accounted for in climate models.

The model's equilibrium sea ice thickness was extremely sensitive to changes in the downward longwave and shortwave fluxes and atmospheric temperature and humidity. Moderate sensitivity was shown to the value of the ocean heat flux. The value of $\langle h_i \rangle$ was insensitive to wind speed, snowfall, and rainfall in the immediate vicinity of the baseline forcing, although significant changes in $\langle h_i \rangle$ occurred for larger variations in wind speed and snowfall.

Six important feedback loops were identified:

1. The surface albedo feedback: A reduction in albedo increases the absorption of solar radiation and therefore the net energy input at the surface, contributing to enhanced melting and a further reduction in albedo. This feedback can involve a reduction in the thickness and/or extent of the sea ice.

2. The conduction feedback: A thinner ice cover experiences greater conduction of heat from the ocean through the ice, contributing to further surface warming and earlier onset of melting.

3. The lead solar flux feedback: Thinner ice allows a greater proportion of the solar flux entering the ocean to be absorbed below the level of the ice where it contributes to warming of the mixed layer and greater basal ablation.

4. The lead fraction feedback: A thinner ice cover experiences greater lateral ice ablation and accretion, resulting in a greater lead fraction in summer and a smaller lead fraction in winter. This allows more solar radiation to be absorbed by the ocean in summer, and insulates the ocean more effectively in winter, both of which contribute to a warmer ocean mixed layer and greater basal ablation.

5. The outgoing longwave flux feedback: The increased outgoing longwave flux from a warmer surface decreases the surface net flux, resulting in cooling.

6. The turbulent flux feedback: A warmer surface reduces the downward sensible and latent heat fluxes (or increases the upward fluxes), which decreases the surface net flux and leads to surface cooling.

The surface albedo, conduction, lead solar flux, and lead fraction feedbacks are positive, or amplifying, while the turbulent flux and outgoing longwave flux feedbacks are negative, or stabilizing. The model also contains other feedback loops which have a smaller influence on the sea ice-lead system. Whenever the system is perturbed, all of the feedback processes participate in the response of the system, but the relative importance of each feedback depends on the nature of the perturbation. Considering the strong influence that sea ice has on global atmospheric and oceanic circulation patterns, it is essential that climate models be able to treat these feedback processes appropriately.

By incorporating a detailed albedo parameterization including melt ponds, this model has addressed some of the weaknesses found in other thermodynamic sea ice models. Because it was designed to be usable in conjunction with an atmospheric radiation model, more attention has been paid to processes occurring at the ice upper surface and less to the underside of the ice and its interactions with the ocean. An obvious improvement to the ocean component of the model would be the use of a variable depth mixed layer model with vertically varying temperature and salinity [e.g., *Mellor and Kantha*, 1989; *Riedlinger and Preller*, 1991]. This would enable a more realistic treatment of the basal heat flux, brine rejection and double diffusion processes, the formation of a stable, cold layer as a results of melt pond drainage, and more realistic mixing of the water in the leads and beneath the ice [*Martin and Kauffman*, 1974; *Perovich and Maykut*, 1990].

It is not possible to include a complete treatment of ice dynamics in a one-dimensional model. However, some improvements could be made to the model in this regard. The most important would be an improved parameterization of sea ice divergence and transport. The divergence rate depends on the wind speed and ocean currents, and also on the thickness of the ice. Time-varying meridional wind and ocean currents, together with momentum flux calculations at the upper and lower surfaces of the ice, could be used to predict meridional ice motion. The adoption of an ice thickness distribution, rather than an ice slab of uniform thickness, would allow for a more realistic treatment of ice rheology. An ice thickness distribution would also allow more detailed flux calculations to be made (*Maykut* [1982] showed that the radiative, conductive, and turbulent fluxes were substantially different for an ice cover of variable thickness than for 3-m multiyear ice) and would almost certainly contain feedback processes not represented in a single-thickness model. *Hibler* [1979] and *Lemke et al.* [1990] demonstrated that the inclusion of dynamics rendered a sea ice model much less sensitive to thermodynamic perturbations due to the interaction of ice dynamics and thermodynamics, which resembles a negative feedback.

Curry and Ebert [1992] coupled this sea ice model to a cloud radiation model to investigate the radiative fluxes at the surface and top of the atmosphere. In that study the turbulent fluxes were prescribed in the sensitivity experiments so that the radiative interactions could be isolated. The addition of an interactive atmospheric boundary layer model would allow many more of the direct interactions and feedbacks between the ice and cloudy boundary layer to be assessed. Earlier studies [*Ebert*, 1984; *Shine and Crane*, 1984] have attempted this coupling using atmospheric models of limited capacity.

The modifications discussed above would add substantial complexity to the sea ice model, even in one dimension. However, the benefits of an improved understanding of many of the relevant physical interactions and feedbacks justify the continued use and improvement of a model such as this. Our future work will focus on improving the model physics, bearing in mind the limitations in the ice dynamics which can be represented in a one-dimensional model. Once the most important processes have been identified, it will be necessary to translate the complex physics into parameterizations which include the essential feedbacks, yet are simple enough to be incorporated into climate models.

NOTATION

Dependent variables

A	lead fraction.
a_p	absorptivity of meltwater pond.
C_T	bulk heat and moisture transfer coefficient over ice.
C_{Tb}	bulk transfer coefficient for ocean heat flux.

D_e effective vapor diffusion coefficient for snow.
F_b ocean heat flux at base of ice slab.
F_c conductive flux.
F_{i0} flux of solar radiation penetrating into the snow-free ice.
F_{lat} latent heat flux from the surface.
F_{net} net flux at the surface (positive downward).
F_p flux of solar radiation penetrating into the meltwater pond.
F_{sens} sensible heat flux from the surface.
F_{wi} flux of solar radiation absorbed by the ocean below the sea ice.
f_{SWdif} fraction of downwelling shortwave flux in the diffuse component.
f_{SWdir} fraction of downwelling shortwave flux in the direct component.
H_p latent heat stored in melt ponds.
h_i depth of the sea ice slab.
h_p depth of meltwater ponds.
h_s depth of the snow layer.
I_0 absorbed fraction of shortwave flux penetrating the snow-free ice.
i_w fraction of solar radiation absorbed by ocean below sea ice
k_i thermal conductivity of sea ice.
k_s thermal conductivity of snow.
P meltwater pond fraction.
S salinity of sea ice.
t_p transmissivity of meltwater pond.
T_i ice temperature.
T_s snow temperature.
T_w temperature of water in leads.
T_{wi} temperature of water beneath ice.
T_0 surface temperature.
z_{i0} roughness length of underside of ice.
α_0 surface albedo.
α_i albedo of bare ice.
α_p albedo of meltwater pond.
α_s albedo of snow.
α_w albedo of open water.
ε_0 surface longwave emissivity.
$(\rho c)_i$ volumetric heat capacity of sea ice.
$(\rho c)_s$ volumetric heat capacity of snow.

Independent variables

z depth (positive downward).
θ_0 solar zenith angle.

Parameters

A_{min} minimum lead fraction, equal to 0.005.
b ocean turbulence parameter, equal to 1.5.
b' atmospheric turbulence parameter, equal to 20.
C_{T0} bulk heat and moisture transfer coefficient for neutral boundary layer, equal to 1.3×10^{-3} for ice, 1.0×10^{-3} for water.
D ice divergence , equal to 4.5×10^{-9} s^{-1}.
d_w depth of ocean mixed layer, equal to 30 m.
f_{RO} fraction of surface meltwater that runs off through cracks and leads, equal to 0.85.
h_{pmax} maximum meltwater pond depth, equal to 0.80 m.
P_{max} maximum meltwater pond fraction, equal to 0.25.
P_{min} minimum meltwater pond fraction, equal to 0.10.
S_i salinity of multiyear sea ice, equal to 3.2 ppt.
ε_s, ε_i longwave emissivity of snow and ice, equal to 0.99 and 0.99, respectively.
ε_w longwave emissivity of water, equal to 0.97.
κ_i shortwave bulk extinction coefficient of sea ice, equal to 1.5 m^{-1}.
ρ_s density of snow, equal to 330 kg m^{-3} for $T < 273.15$ K and 450 kg m^{-3} for $T = 273.15$ K.

Specified forcing variables

F_{LW} downward longwave flux at the surface.
F_{SW} downward shortwave flux at the surface.
F_{ocean} heat flux from the ocean beneath the mixed layer.
q_a air specific humidity.
RF rainfall at the surface.
SF snowfall at the surface.
T_a air temperature.
u_a wind speed at 10 m.
w_j fractional solar flux in spectral interval j, j=1, 2, 3, 4.

Constants

c_p specific heat capacity of dry air at const. pressure, equal to 1005 J kg^{-1} K^{-1}.
g gravitational acceleration, equal to 9.81 m s^{-2}.
$k_{i,f}$ thermal conductivity of pure sea ice, equal to 2.034 W m^{-1} K^{-1}.
L_{fb} volumetric heat of fusion at bottom of ice slab, equal to 2.679×10^8 J m^{-3}.
L_{fi} volumetric heat of fusion for sea ice, equal to 3.014×10^8 J m^{-3}.
L_{fs} volumetric heat of fusion for snow, equal to 1.097×10^8 J m^{-3}.
L_s latent heat of sublimation, equal to 2.834×10^6 J m^{-3}.
L_v latent heat of vaporization, equal to 2.501×10^6 J m^{-3}.
R_d gas constant for dry air, equal to 287.05 J kg^{-1} K^{-1}.
R_v gas constant for water vapor , equal to 461.51 J kg^{-1} K^{-1}.
ρ_a density of dry air, equal to 1.275 kg m^{-3}.
ρ_i density of sea ice, equal to 900 kg m^{-3}.
ρ_w density of sea water at 0°C, equal to 1026 kg m^{-3}.
$(\rho c)_{i,f}$ volumetric heat capacity of pure ice at 273 K, equal to 1.883×10^6 J m^{-3} K^{-1}.
$(\rho c)_w$ volumetric heat capacity of water, equal to 4.190×10^6 J m^{-3} K^{-1}.
σ Stefan-Boltzmann constant, equal to 5.67×10^{-8} W m^{-2} K^{-4}.

Acknowledgments. The authors wish to thank the anonymous reviewers for their comments and suggestions. Support for this research was provided by the National Science Foundation under grants DPP-8858830 and DPP-8820905, by the Office of Naval Research under grant N00014-91-J-1387, and by the Department of Energy National Institute for Global and Environmental Change, South Central Region.

REFERENCES

Aagaard, K., L.K. Coachman, and E. Carmack, On the halocline of the Arctic Ocean, *Deep Sea Res., Part A, 28*, 529-545, 1981.

Aagaard, K., and P. Greisman, Towards new mass and heat budgets for the Arctic Ocean, *J. Geophys. Res., 80*, 3821-3827, 1975.

Abels, G., Measurement of the snow density at Ekaterinburg during the winter of 1890-1891, *Akad. Nauk, Mem., 69*, 1-24, 1892.

Anderson, E.A., A point energy and mass balance model of a snow cover, *NOAA Tech. Rep. NWS 19*, Natl. Oceanic and Atmos. Admin., Washington, D.C., 1976.

Andreas, E.L., A theory for the scalar roughness and the scalar transfer coefficients over snow and sea ice, *Boundary Layer Meteorol., 38*, 159-184, 1987.

Andreas, E.L., and B. Murphy, Bulk transfer coefficients for heat and momentum over leads and polynyas, *J. Phys. Oceanogr., 16*, 1875-1883, 1986.

Asselin, R., Northern hemisphere sea ice climatology and analyses, 19 pp., Div. de Rech. en Prévision Numér., Atmos. Environ. Serv., Dorval, Québec, Canada, 1977.

Badgley, F.I., Heat balance at the surface of the Arctic Ocean, in Proceedings of the Symposium on the Arctic Heat Budget and Atmospheric Circulation, edited by J.O. Fletcher, *RM-5233-NSF*, pp. 215-246, Rand Corp., Santa Monica, Calif., 1966.

Banks, H.C., and E.N. Partanen, Meteorological observations, in Scientific Studies at Fletcher's Ice Island, T-3, 1952-1955, vol. II., edited by V. Bushnell, *AFCRC-TR-59-232(2)*, pp. 1-49, Air Force Cambridge Res. Lab., Cambridge, Mass., 1959.

Barry, R.G., The present climate of the Arctic Ocean and possible past and future states, in *The Arctic Seas. Climatology, Oceanography, Geology, and Biology*, edited by Y. Herman, pp. 1-46, Van Nostrand Reinhold, New York, 1989.

Bourke, R.H., and R.P. Garrett, Sea ice thickness distribution in the Arctic Ocean, *Cold Reg. Sci. Technol., 13*, 259-280, 1987.

Briegleb, B.P., P. Minnis, V. Ramanathan, and E.F. Harrison, Comparison of clear-sky albedos inferred from satellite observations and model computations, *J. Clim. Appl. Meteorol., 25*, 214-226, 1986.

Budyko, M.I., Polar ice and climate (in Russian), *Izv. Akad. Nauk SSSR, Ser. Geogr., 6*, 5-36, 1962. (English translation, Proceedings of the Symposium on the Arctic Heat Budget and Atmospheric Circulation, edited by J.O. Fletcher, *RM-5233-NSF*, pp. 3-21, Rand Corporation, Santa Monica, Calif., 1966.)

Carsey, F.J., Arctic sea ice distribution at end of summer 1973-1976 from satellite microwave data, *J. Geophys. Res., 87*, 5809-5835, 1982.

Cavalieri, D.J., B.A. Burns, and R.G. Onstott, Investigation of the effects of summer melt on the calculation of sea ice concentration using active and passive microwave data, *J. Geophys. Res., 95*, 5359-5369, 1990.

Chernigovskii, N.T., Radiation regime of the central Arctic Basin, *Probl. Arct. Antarc.*, no. 29, 3-11, 1968.

Choudhury, B.J., and A.T.C. Chang, The albedo of snow for partially cloudy skies, *Boundary Layer Meteorol., 20*, 371-389, 1981.

Chukanin, K.I., Aerometeorology, in *Observational Data of the Scientific-Research Drifting Station of 1950-1951*, vol. III, edited by M.M. Somov, Morskoi Transport, St. Petersburg, Russia, 1954. (English translation by E.R. Hope, American Meteorological Society, Boston, Mass. Available as NTIS AD117139 from Natl. Tech. Inf. Serv., Springfield, Va.)

Colony, R., and A.S. Thorndike, An estimate of the mean field of Arctic sea ice motion, *J. Geophys. Res., 89*, 10,623-10,629, 1984.

Comiso, J.C., Arctic multiyear ice classification and summer ice cover using passive microwave satellite data, *J. Geophys. Res., 95*, 13,411-13,422, 1990.

Cox, G.F.N., and W.F. Weeks, Salinity variations in sea ice, *J. Glaciol., 13*, 109-120, 1974.

Crane, R.G., and R.G. Barry, The influence of clouds on climate with a focus on high latitude interactions, *J. Climatol., 4*, 71-93, 1984.

Curry, J.A., and E.E. Ebert, Annual cycle of radiation fluxes over the Arctic Ocean: Sensitivity to cloud optical properties, *J. Clim., 5*, 1267-1280, 1992.

Curry, J.A., and G.F. Herman, Infrared radiative properties of summertime Arctic stratus clouds, *J. Clim. Appl. Meteorol., 24*, 526-538, 1985.

Doronin, Yu. P., On the heat balance of the central Arctic (in Russian), *Tr. Arkt. Antarkt. Nauchno Issled. Inst., 253*, 178-184, 1963.

Ebert, E.E., Radiative interactions between Arctic sea ice and boundary layer stratus clouds, M.S. thesis, Univ. of Wis., Madison, 1984.

Ebert, E.E., and J.A. Curry, A parameterization of ice cloud optical properties for climate models, *J. Geophys. Res., 97*, 3831-3836, 1992.

Flato, G.M., and W.D. Hibler III, On modeling pack ice as a cavitating fluid, *J. Phys. Oceanogr., 22*, 626-651, 1992.

Fleming, G.H., and A.J. Semtner, Jr., A numerical study of interannual ocean forcing on Arctic ice, *J. Geophys. Res., 96*, 4589-4603, 1991.

Francis, J.A., T.P. Ackerman, K.B. Katsaros, R.J. Lind, and K.L. Davidson, A comparison of radiation budgets in the Fram Strait summer marginal ice zone, *J. Climate, 4*, 218-235, 1991.

Grenfell, T.C., A theoretical model of the optical properties of sea ice in the visible and near infrared, *J. Geophys. Res., 88*, 9723-9735, 1983.

Grenfell, T.C., and G.A. Maykut, The optical properties of ice and snow in the Arctic Basin, *J. Glaciol., 18*, 445-463, 1977.

Grenfell, T.C., and D.K. Perovich, Spectral albedos of sea ice and incident solar irradiance in the southern Beaufort Sea, *J. Geophys. Res., 89*, 3573-3580, 1984.

Häkkinen, S., and G.L. Mellor, One hundred years of Arctic ice cover variations as simulated by a one-dimensional, ice-ocean model, *J. Geophys. Res., 95*, 15,959-15,969, 1990.

Harshvardhan, R. Davies, D.A. Randall, and T.G. Corsetti, A fast radiation parameterization for atmospheric circulation models, *J. Geophys. Res., 92*, 1009-1016, 1987.

Harvey, L.D.D., Development of a sea ice model for use in zonally averaged energy balance climate models, *J. Clim., 1*, 1221-1238, 1988*a*.

Harvey, L.D.D., On the role of high latitude ice, snow, and vegetation feedbacks in the climatic response to external forcing changes, *Clim. Change, 13*, 191-224, 1988*b*.

Harvey, L.D.D., Testing alternative parameterizations of lateral melting and upward basal heat flux in a thermodynamic sea ice model, *J. Geophys. Res., 95*, 7359-7365, 1990.

Hibler, W.D., III, A dynamic thermodynamic sea ice model, *J. Phys. Oceanogr., 9*, 815-846, 1979.

Hibler, W.D., III, and K. Bryan, A diagnostic ice-ocean model, *J. Phys. Oceanogr., 17*, 987-1015, 1987.

Hibler, W.D., III, and J.E. Walsh, On modeling seasonal and interannual fluctuations of Arctic sea ice, *J. Phys. Oceanogr., 12*, 1514-1523, 1982.

Huschke, R.E., Arctic cloud statistics from "air-calibrated" surface weather observations, *RM-6173-PR*, Rand Corp., Santa Monica, Calif., 1969.

Ingram, W.J., C.A. Wilson, and J.F.B. Mitchell, Modeling climate change: An assessment of sea ice and surface albedo feedbacks, *J. Geophys. Res., 94*, 8609-8622, 1989.

Kantha, L.H., and G.L. Mellor, A two-dimensional coupled ice-ocean model of the Bering Sea marginal ice zone, *J. Geophys. Res., 94*, 10,921-10,935, 1989.

Koenig, L.S., K.R. Greenaway, M. Dunbar, and G. Hattersley-Smith, Arctic ice islands, *Arctic, 5*, 67-103, 1952.

Koerner, R.M., The mass balance of the sea ice of the Arctic Ocean, *J. Glaciol., 12*, 173-185, 1973.

Lacis, A.A. and J.E. Hansen, A parameterization for the absorption of solar radiation in the earth's atmosphere, *J. Atmos. Sci., 31*, 118-133, 1974.

Leavitt, E., M. Albright, and F. Carsey, Report on the AIDJEX Meteorological Experiment, *AIDJEX Bull., 39*, pp. 121-148, Univ. of Wash., Seattle, 1978.

Ledley, T.S., Sea ice: Multiyear cycles and white ice, *J. Geophys. Res., 90*, 5676-5686, 1985.

Ledley, T.S., Development of a new sea ice growth and lead parameterization, *Clim. Dyn., 2*, 91-100, 1987.

Ledley, T.S., A coupled energy balance climate-sea ice model: Impact of sea ice and leads on climate, *J. Geophys. Res., 93*, 15,919-15,932, 1988.

Ledley, T.S., Snow on sea ice: Competing effects in shaping climate, *J. Geophys. Res., 96*, 17,195-17,208, 1991.

Lemke, P., and T.O. Manley, The seasonal variation of the mixed layer and the pycnocline under polar sea ice, *J. Geophys. Res., 89*, 6494-6504, 1984.

Lemke, P., W.B. Owens, and W.D. Hibler III, A coupled sea ice-mixed layer pycnocline model for the Weddell Sea, *J. Geophys. Res., 95*, 9513-9525, 1990.

Loshchilov, V.S., Snow cover over ice in the central Arctic (in Russian), *Probl. Ark. Antark., 17*, 36-45, 1964.

Louis, J.-F., A parameteric model of vertical eddy fluxes in the atmosphere, *Boundary Layer Meteorol., 17*, 187-202, 1979.

Makshtas, A.P., The heat budget of Arctic ice in the winter, Arct. Antarc. Res. Inst., St. Petersburg, Russia, 1984. (English translation edited by E.L. Andreas, 1991. Available from Int. Glaciol. Soc., Cambridge, England)

Manabe, S., and R.J. Stouffer, Sensitivity of a global climate model to an increase of CO_2 concentration in the atmosphere, *J. Geophys. Res., 85*, 5529-5554, 1980.

Marshunova, M.S., Principal characteristics of the radiation balance of the underlying surface and of the atmosphere in the Arctic (in Russian), *Tr. Ark. Antark. Nauchno Issled. Inst., 229*, 1961. (English translation, *RM-5003-PR*, Rand Corp., Santa Monica, Calif., 1966.)

Martin, S., and P. Kauffman, The evolution of under-ice melt ponds, or double diffusion at the freezing point, *J. Fluid Mech., 64*, 507-527, 1974.

Maykut, G.A., Energy exchange over young sea ice in the central Arctic, *J. Geophys. Res., 83*, 3646-3658, 1978.

Maykut, G.A., Large-scale heat exchange and ice production in the central Arctic, *J. Geophys. Res., 87*, 7971-7984, 1982.

Maykut, G.A., Surface heat and mass balance, in *The Geophysics of Sea Ice*, edited by N. Untersteiner, pp.395-463, Plenum, New York, 1986.

Maykut, G.A., and D.K. Perovich, MIZEX 84 heat and mass balance data, *Rep. APL-UW 12-85*, Appl. Phys. Lab., Univ. of Wash., Seattle, 1985.

Maykut, G.A., and D.K. Perovich, The role of shortwave radiation in the summer decay of a sea ice cover, *J. Geophys. Res., 92*, 7032-7044, 1987.

Maykut, G.A., and N. Untersteiner, Some results from a time dependent thermodynamic model of sea ice, *J. Geophys. Res., 76*, 1550-1575, 1971.

McLaren, A.S., Analysis of the under-ice topography in the Arctic Ocean, as recorded by USS *Nautilus* in 1958 and USS *Queenfish* in 1970, Ph.D. dissertation, Dep. of Geogr., Univ. of Colo., Boulder, 1986.

McPhee, M., and N. Untersteiner, Using sea ice to measure vertical flux in the ocean, *J. Geophys. Res., 87*, 2071-2074, 1982.

Mellor, G.L. and L. Kantha, An ice-ocean coupled model, *J. Geophys. Res.*, 94, 10,937-10,954, 1989.

Mitchell, A.R., and D.F. Griffiths, *The Finite Difference Method in Partial Differential Equations*, John Wiley, New York, 1980.

Moritz, R.E., The ice budget of the Greenland Sea, *Tech. Rep. APL-UW TR 8812*, Appl. Phys. Lab., Univ. of Wash., Seattle, 1988.

Nazintsev, Yu.L., Thermal balance of the surface of the perennial ice cover in the central Arctic (in Russian), *Tr. Ark. Antark. Nauchno Issled. Inst., 267*, 110-126, 1964.

Neumann, G., and W.J. Pierson, Jr., *Principles of Physical Oceanography*, Prentice Hall, Englewood Cliffs, N.J., 1966.

Nikoforov, Ye.,G., V.V. Lukin, A.P. Makshtas, and V.D. Grishchenko, USSR proposal for an international Arctic drifting station, in Report of the Fourth Session of the Working Group on Sea Ice and Climate, *WCRP-41, WMO/TD 377*, Annex F, World Clim. Res. Program, World Meteorol. Organ., Geneva, 1990.

Ono, N., Specific heat and heat of fusion of sea ice, in *Physics of Snow and Ice, vol. 1*, edited by H. Oura, pp. 599-610, Institute of Low Temperature Science, Hokkaido, Japan, 1967.

Oort, A.H., Global atmospheric circulation statistics, 1958-1973, *NOAA Prof. Pap. 14*, Natl. Ocean. Atmos. Admin., Washington, D.C., 1983.

Parkinson, C.L., and W.M. Kellogg, Arctic sea ice decay simulated for a CO_2-induced temperature rise, *Clim. Change, 2*, 149-162, 1979.

Parkinson, C.L., and W.M. Washington, A large-scale numerical model of sea ice, *J. Geophys. Res., 84*, 311-337, 1979.

Perovich, D.K., and G.A. Maykut, Solar heating of a stratified ocean in the presence of a static ice cover, *J. Geophys. Res., 95*, 18,233-18,245, 1990.

Riedlinger, S.H., and R.H. Preller, The development of a coupled ice-ocean model for forecasting ice conditions in the Arctic, *J. Geophys. Res., 96*, 16,955-16,977, 1991.

Robinson, D.A., G. Scharfen, R.G. Barry, and G. Kukla, Analysis of interannual variations of snow melt on Arctic sea ice mapped from meteorological satellite imagery, in Large Scale Effects of Seasonal Snow Cover, *IAHS Publ. 166*, 315-327, 1987.

Robock, A., The seasonal cycle of snow cover, sea ice and surface albedo, *Mon. Wea. Rev., 108*, 267-285, 1980.

Ross, B., and J.E. Walsh, A comparison of simulated and observed fluctuations in summertime Arctic surface albedo, *J. Geophys. Res., 92*, 13,115-13,125, 1987.

Scharfen, G., R.G. Barry, D.A. Robinson, G. Kukla, and M.C. Serreze, Large-scale patterns of snow melt on Arctic sea ice mapped from meteorological satellite imagery, *Ann. Glaciol., 9*, 1-6, 1987.

Schlesinger, M.E., Analysis of results from energy balance and radiative-convective models, in Projecting the Climatic Effects of Increasing Carbon Dioxide, edited by M.C. MacCracken and F.M. Luther, *DOE/ER-0237*, pp. 81-147, U.S. Dep. of Energy, Washington, D.C., 1985.

Schwarzacher, W., Pack ice studies in the Arctic Ocean, *J. Geophys. Res., 64*, 2357-2367, 1959.

Semtner, A.J., Jr., A model for the thermodynamic growth of sea ice in numerical investigations of climate, *J. Phys. Oceanogr., 6*, 379-389, 1976.

Semtner, A.J., Jr., On modelling the seasonal thermodynamic cycle of sea ice in studies of climatic change, *Clim. Change, 6*, 27-37, 1984.

Semtner, A.J., Jr., A numerical study of sea ice and ocean circulation in the Arctic, *J. Phys. Oceanogr., 17*, 1077-1099, 1987.

Shine, K.P., and R.G. Crane, The sensitivity of a one-dimensional thermodynamic sea ice model to changes in cloudiness, *J. Geophys. Res., 89*, 10,615-10,622, 1984.

Shine, K.P., and A. Henderson-Sellers, The sensitivity of a thermodynamic ice model to changes in surface albedo parameterization, *J. Geophys. Res., 90*, 2243-2250, 1985.

Slingo, A., A GCM parameterization for the shortwave radiative properties of water clouds, *J. Atmos. Sci., 46*, 1419-1427, 1989.

Takano, Y., and K.-N. Liou, Solar radiative transfer in cirrus clouds, I, Single-scattering and optical properties of hexagonal ice crystals, *J. Atmos. Sci., 46*, 3-19, 1989.

Untersteiner, N., On the mass and heat budget of Arctic sea ice, *Arch. Meteorol. Geophys. Bioklimatol., Ser. A, 12*, 151-182, 1961.

Untersteiner, N., Calculations of temperature regime and heat budget of sea ice in the central Arctic, *J. Geophys. Res., 69*, 4755-4766, 1964.

Vinje, T., and Ø. Finnekasa, The ice transport through the Fram Strait, *Skr. Nor. Polarinst., 186*, 1986.

Vowinckel, E., and S. Orvig, The climate of the North Polar Basin, in *Climates of the Polar Regions,World Survey of Climatology*, vol. 14, edited by S. Orvig, Elsevier, New York, 1970.

Walsh, J.E., The role of sea ice in climatic variability: Theories and evidence, *Atmos. Ocean, 3*, 229-242, 1983.

Washington, W.M., and G.A. Meehl, General circulation model experiments on the climatic effects due to a doubling and quadrupling of carbon dioxide concentrations, *J. Geophys. Res., 88*, 6600-6610, 1983.

Washington, W.M., A.J. Semtner, C.L. Parkinson, and L. Morrison, On the development of a season change sea-ice model, *J. Phys. Oceanogr., 6*, 679-685, 1976.

World Climate Research Program (WCRP), Report of the second session of the working group on sea ice and climate , *WCP-128, WMO/TD 127*, World Meteorol. Organ., Geneva, 1987.

Weeks, W.F., Sea ice conditions in the Arctic, *AIDJEX Bull., 34*, 173-205, Univ. of Wash., Seattle, 1976.

Weeks, W.F., and S.F. Ackley, The growth, structure, and properties of sea ice, in *The Geophysics of Sea Ice*, edited by N. Untersteiner, pp. 9-164, Plenum, New York, 1986.

Wettlaufer, Heat flux at the ice-ocean interface, *J. Geophys. Res., 96*, 7215-7236, 1991.

Wiscombe, W.J. and S.G. Warren, A model for the spectral albedos of snow, I, Pure snow, *J. Atmos. Sci., 37*, 2712-2733, 1980.

Yen, Y.-C., Recent studies on snow properties, *Adv. Hydrosci., 5*, 173-214, 1969.

J.A. Curry, Department of Aerospace Engineering Sciences, Campus Box 429, University of Colorado, Boulder, CO 80309.

E.E. Ebert, Bureau of Meteorology Research Centre, GPO Box 1289K, Melbourne, Victoria 3000, Australia.

(Received February 27, 1992;
revised February 8, 1993;
accepted February 19, 1993.)